

*Annual Review of Materials Research***Recent Advances in Solid-State  
Nuclear Magnetic Resonance  
Techniques for Materials  
Research****Po-Hsiu Chien,<sup>1,2</sup> Kent J. Griffith,<sup>3</sup> Haoyu Liu,<sup>1</sup>  
Zhehong Gan,<sup>2</sup> and Yan-Yan Hu<sup>1,2</sup>**<sup>1</sup>Department of Chemistry and Biochemistry, Florida State University, Tallahassee, Florida 32306, USA; email: yhu@fsu.edu<sup>2</sup>Center of Interdisciplinary Magnetic Resonance, National High Magnetic Field Laboratory, Tallahassee, Florida 32310, USA<sup>3</sup>Departments of Chemistry and Materials Science and Engineering, Northwestern University, Evanston, Illinois 60208, USA

Annu. Rev. Mater. Res. 2020. 50:493–520

First published as a Review in Advance on  
May 15, 2020The *Annual Review of Materials Research* is online at  
matsci.annualreviews.org<https://doi.org/10.1146/annurev-matsci-091019-011049>Copyright © 2020 by Annual Reviews.  
All rights reserved**ANNUAL  
REVIEWS CONNECT**[www.annualreviews.org](http://www.annualreviews.org)

- Download figures
- Navigate cited references
- Keyword search
- Explore related articles
- Share via email or social media

**Keywords**

solid-state NMR, spectral resolution, sensitivity enhancement, dynamics, DNP, MRI

**Abstract**

Establishing structure–property correlations is of paramount importance to materials research. The ability to selectively detect observable magnetization from transitions between quantized spin states of nuclei makes nuclear magnetic resonance (NMR) spectroscopy a powerful probe to characterize solids at the atomic level. In this article, we review recent advances in NMR techniques in six areas: spectral resolution, sensitivity, atomic correlations, ion dynamics, materials imaging, and hardware innovation. In particular, we focus on the applications of these techniques to materials research. Specific examples are given following the general introduction of each topic and technique to illustrate how they are applied. In conclusion, we suggest future directions for advanced solid-state NMR spectroscopy and imaging in interdisciplinary research.

## 1. INTRODUCTION

Nuclear magnetic resonance (NMR) spectroscopy and imaging use nuclear spins as probes of local atomic and electronic structures. Solution-state NMR is a proven and ubiquitous technique for molecular structure elucidation in biochemistry, organic chemistry, and pharmaceutical research. Recent decades have witnessed the rapid development of solid-state NMR. Although solid-state NMR obeys the same principles as solution NMR, anisotropic and through-space NMR interactions such as chemical shifts and dipolar, quadrupolar, and paramagnetic couplings are not averaged out in solids due to the absence of fast, isotropic molecular motion that occurs in liquids. Consequently, solid-state NMR typically suffers from poor spectral resolution with low sensitivity, though these challenges are being addressed (1, 2).

With challenges come opportunities: Due to the lack of sufficiently fast motion in solids, many important NMR interactions are retained, providing rich information on spatial proximity and dynamics. Materials properties are regulated by the synergy among functional sites, their local environments, and the spatial arrangement relative to other structural motifs. From this perspective, NMR correlation spectroscopy, which in part relies on the strength of coupling between adjacent nuclei through bonds or space, can offer precise information on the connectivity of the structural framework and the distribution/concentration of functional groups (3). In addition, NMR offers a complement of powerful tools such as relaxometry and pulsed field gradient (PFG) measurements to probe dynamics in materials for both long-range and short-range motion (4). In addition, the activation energy associated with different types of motion (e.g., translational, rotational) can be quantified via variable-temperature NMR measurements and used to evaluate models of ion transport and local dynamics (5).

Adding spatial resolution to solid-state NMR spectroscopy yields magnetic resonance imaging (MRI). MRI is used widely in fundamental research in the health-related sciences, and clinical MRI is a standard practice in medical diagnosis. MRI is emerging as an important technique in materials research to understand systems on different length scales. MRI can noninvasively access qualitative and quantitative information on the distribution of chemical species, following the response of chemical reactions to external stimuli such as electromagnetic fields (6). Materials MRI presents a different set of technical challenges compared to clinical MRI, involving a much more diverse set of nuclei, electronic properties, and environmental conditions. Electronically conductive components often result in large image distortions due to limited penetration depth of the conductive region by radio frequency pulses that are used to perturb nuclear spins in NMR and MRI. For experiments beyond  $^1\text{H}$  MRI, low sensitivity typically requires a long acquisition time and also compromises image resolution. Recently, it has been demonstrated that  $^7\text{Li}$  MRI can yield undistorted 3D images of the Li distribution in solid electrolytes even in the presence of metallic lithium (7). This opens up the possibility of conducting in situ MRI experiments on solid-state rechargeable lithium-ion batteries. The advancement of solid-state NMR/MRI for materials studies also relies on the development of NMR probes and rotors. Recent developments in NMR hardware allow investigation of materials under extreme conditions such as high pressure and temperature. Beyond all of these to-be-discussed topics in this short review, it is worth noting that the potential of machine learning (ML) to determine structures from chemical shifts has been demonstrated recently (8), a new direction of ML-assisted NMR for materials research.

In this review, we focus on recent advancements in solid-state NMR techniques and hardware specifically oriented toward materials research. Select examples from the literature are included in an attempt to illustrate how these techniques are applied and what new insights can be obtained. For a review of basic NMR concepts, the readers are referred to several excellent books listed in the Literature Cited (9–15).

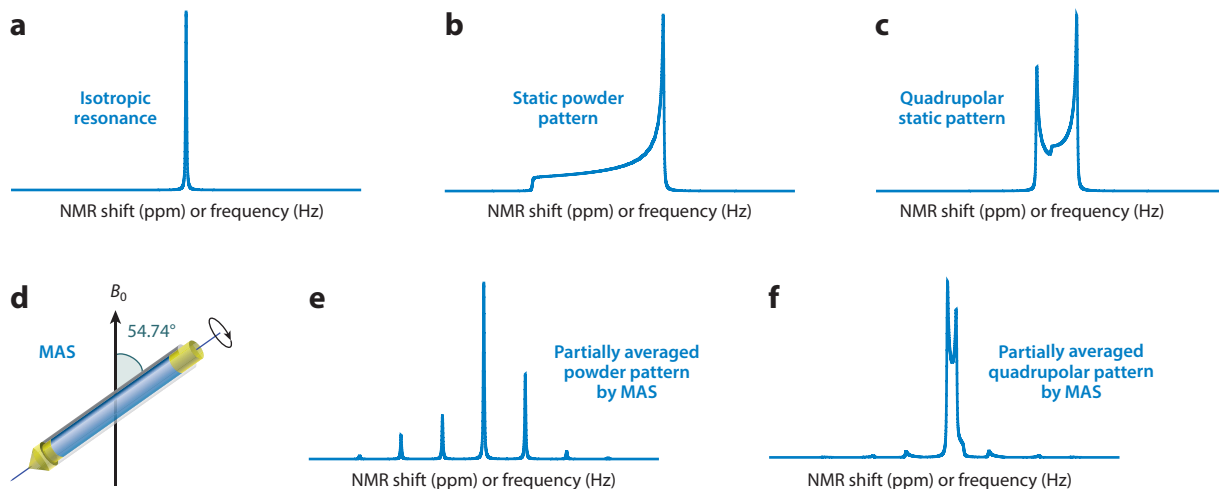


**Figure 1**

Solid-state nuclear magnetic resonance (NMR) spectroscopy. (a) An example of the isotropic NMR resonance characteristic of local spin environments free of any isotropic effects typically observed in solution NMR. (b) A representative solid-state NMR powder pattern illustrating the shift anisotropy determined by distribution of nuclear spin (molecular) orientations. (c) An example of solid-state NMR resonance broadened by quadrupolar coupling. (d) Schematic of the magic-angle spinning (MAS) technique in which the solid-state NMR sample container, also known as the rotor, is tilted at an angle of  $\cos^{-1}(1/\sqrt{3}) \approx 54.74^\circ$  with respect to the external magnetic field axis ( $B_0$ ). (e) NMR powder pattern in panel b transformed into an isotropic resonance and spinning sideband manifolds under the MAS condition. A MAS rate much greater than the span of shift anisotropy yields a pure isotropic spectrum as shown in panel a. (f) Partially averaged quadrupolar pattern in panel c with MAS, showing only the residual effect from second-order quadrupolar couplings, which cannot be removed by MAS alone. Panel d adapted with permission from Reference 19; copyright 2015 American Chemical Society.

## 2. IMPROVING SPECTRAL RESOLUTION

NMR spectra of solids exhibit line broadening due to crystallite orientation-dependent anisotropic interactions such as chemical shifts and dipolar coupling (16) (Figure 1b,e). By contrast, these anisotropic effects are largely removed by fast isotropic molecular tumbling in solution-state NMR (Figure 1a). Rapid spinning of solids at an angle of  $54.74^\circ$ , also known as magic-angle spinning (MAS) (Figure 1d), with respect to the direction of the external magnetic field ( $B_0$ ) mechanically and partially averages the anisotropic broadening, leading to improved spectral resolution (17–19) (Figure 1e,f). Complete removal of the effects of anisotropic interactions with MAS alone requires sample spinning rates much larger than the amplitude of the dominant interactions (often kilohertz or megahertz). For solid-state  $^1\text{H}$  NMR, fast MAS is needed to suppress the strong  $^1\text{H}$ – $^1\text{H}$  homonuclear dipolar couplings. Several recent studies have employed ultrafast MAS up to 100–110 kHz (20–24). The current record for reported MAS rate is 126 kHz (25). However, faster spinning is typically achieved by reducing the NMR rotor diameter and sample volume, hence compromising sensitivity. For nuclei with low natural abundance and low magnetogyric ratio ( $\gamma$ ), for example,  $^{15}\text{N}$  or  $^{29}\text{Si}$ , maintaining sample volume while pursuing fast spinning becomes important for obtaining satisfactory sensitivity. Chen et al. (26) have recently demonstrated a novel spherical sample container with the potential for a higher limit of spinning speed up to 150 kHz and improved detection sensitivity compared to the traditional cylindrical design.

For nuclei with spin  $I > 1/2$ , e.g.,  $^2\text{H}$  ( $I = 1$ ),  $^{23}\text{Na}$  ( $I = 3/2$ ),  $^{17}\text{O}$  ( $I = 5/2$ ), and  $^{93}\text{Nb}$  ( $I = 9/2$ ), the nucleus is nonspherical and thus possesses a quadrupole moment. The interaction between the quadrupole moment and the nonvanishing electric field gradient (EFG) induced by asymmetric distribution of electron density around the nucleus, i.e., quadrupolar coupling, further

complicates solid-state NMR spectra (**Figure 1c,f**) (27). Quadrupolar couplings are typically on the order of megahertz and can approach the magnitude of the Zeeman interaction that underlies the phenomenon of NMR. The majority of NMR-active ( $I > 0$ ) nuclei are half-integer quadrupolar nuclei. For these quadrupolar nuclei, quadrupolar coupling does not affect the central transition (CT;  $1/2 \leftrightarrow -1/2$ ) in the first order, giving rise to relatively narrow peaks with broadening only from the second-order quadrupolar effect (27–30), where first and second order refer to perturbation terms of the full quadrupolar Hamiltonian (28). The so-called satellite-transition (ST;  $-I \leftrightarrow -I + 1$  to  $I - 1 \leftrightarrow I$  in integer steps, excluding  $1/2 \leftrightarrow -1/2$ ) signals of quadrupolar nuclei typically spread over many megahertz. MAS can further narrow the CT signal, whereas the ST signals typically appear as small spinning sidebands (SSBs) often buried in the baseline. It is worth noting that MAS does not average out the second-order quadrupolar coupling completely because the angular dependence of the second-order effects is different from the first-order effects. Since second-order quadrupolar coupling is inversely proportional to the Larmor frequency ( $\omega$ ) (15), acquiring the spectrum of a quadrupolar resonance at higher external magnetic fields ( $\omega \propto B_0$ ) reduces the linewidth. This effect is illustrated in **Figure 2a**, showing improved  $^{27}\text{Al}$  ( $I = 5/2$ ) NMR spectral resolution in model structures of the ceramic  $\beta\text{-Si}_{3-x}\text{Al}_x\text{O}_x\text{N}_{4-x}$  with increasing magnetic field strength due to reduced quadrupolar coupling effects (31).

The peak positions in MAS spectra of quadrupolar nuclei are determined by two contributions, the chemical shift ( $\propto B_0$ ) and the quadrupolar shift from second-order quadrupolar splitting ( $\propto B_0^{-1}$ ). With their different magnetic field dependencies, acquiring spectra at multiple magnetic fields is a useful way to resolve the two contributions. 2D multiple-quantum MAS (MQMAS) is a powerful and widely used technique for obtaining pure isotropic spectra of quadrupolar nuclei (32, 33). For crystalline samples, two-dimensional MQMAS NMR separates the isotropic spectra from the quadrupolar-broadened spectra, allowing the determination of the quadrupolar coupling constant ( $C_Q$ ) and asymmetry ( $\eta$ ) for distinct sites of interest (**Figure 2c**). For disordered samples, MQMAS spreads the distributions of the chemical and quadrupolar shifts into two dimensions, which allows the determination of the relative weighting between the two (34). A variant, satellite-transition MAS (STMAS) (35, 36) can be more efficient than MQMAS because the former relies on the excitation of single-quantum STs, which have a higher excitation efficiency than multiple-quantum excitations. However, the averaging of the STs requires precise setting of the magic-angle and stable spinning speed, making STMAS less robust than MQMAS (36). Other methods such as double rotation (37) and dynamic-angle spinning (38) exist, but they are not discussed further here as they are not widely available due to more demanding hardware requirements.

Paramagnetic materials often exhibit large shift anisotropy as a result of the nucleus–electron spin dipolar coupling. Acquiring a clean, solid-state NMR spectrum with only isotropic shifts can be challenging (39). The large anisotropy ( $>1$  MHz) cannot be resolved simply by MAS, obscuring an accurate determination of isotropic shifts due to the overlap of multifold SSBs. Hung et al. (40) developed a novel 2D NMR method known as projection magic-angle turning phase-adjusted sideband separation (pjMATPASS) to overcome this problem. The pjMATPASS method is built on the combination of respective features from magic-angle turning (MAT) (41) and phase-adjusted sideband separation (PASS) (42) under MAS conditions. The 2D MAT technique (41) obtains isotropic shifts by removing chemical shift anisotropy (CSA) through three discrete time evolution segments in the indirect time dimension ( $t_1$ ) that last for one-third of a rotor cycle, i.e.,  $120^\circ$  apart in rotor phase (43). The sum of the CSA modulation from the three  $t_1$  segments, i.e., a full rotor cycle ( $360^\circ$ ), is zero. The 2D PASS method encodes only CSA in  $t_1$  (42), and a few  $t_1$  increments extending up to one rotor cycle are sufficient considering that CSA modulation is periodic with the rotor cycle. However, the solution for such encoding requires nonlinear time increments of the pulses. The hybrid between MAT and PASS, namely, MATPASS, defers the start of

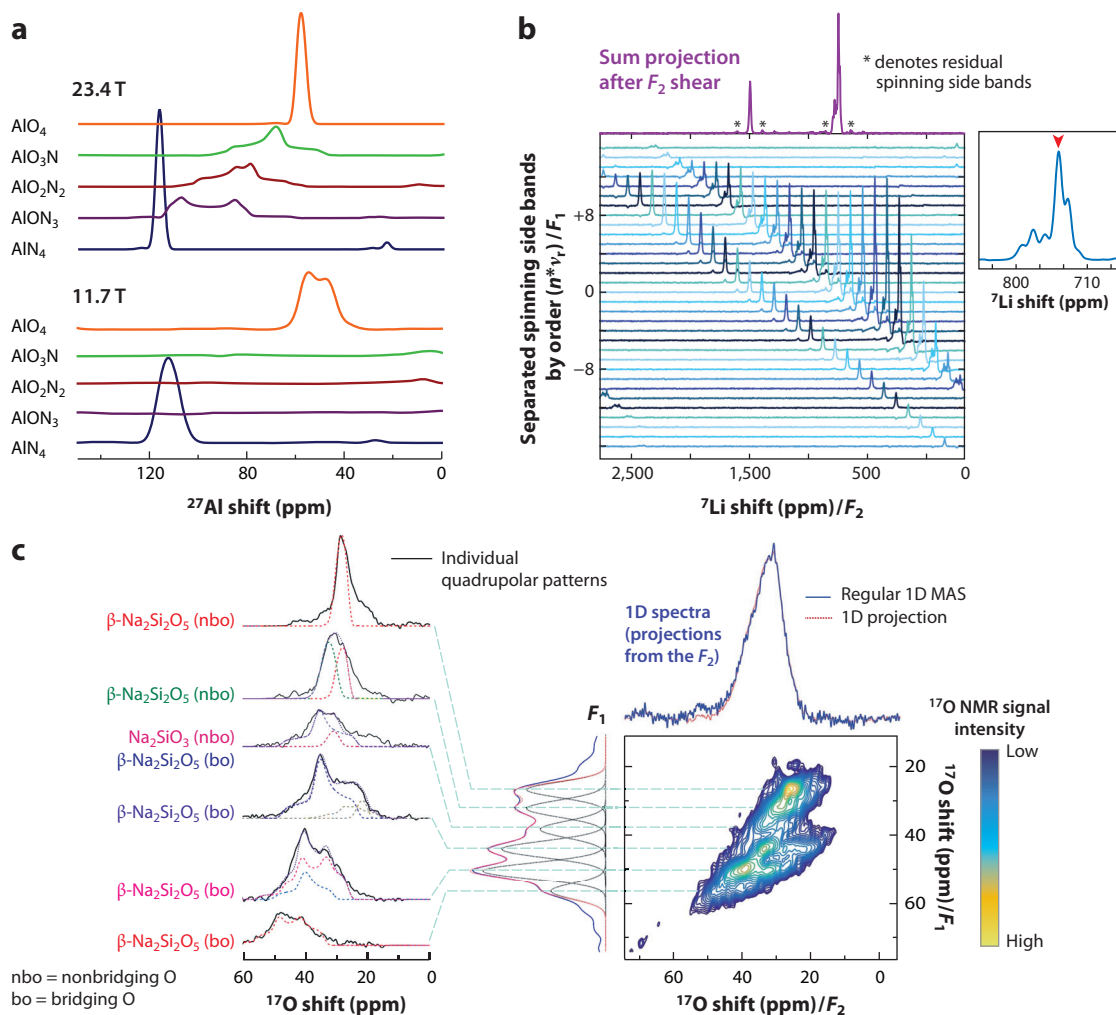


**Figure 2**

Techniques for improving spectral resolution of solid-state nuclear magnetic resonance (NMR). (a) High magnetic field: an example demonstrating reduced quadrupolar broadening of <sup>27</sup>Al (spin-3/2) NMR resonances in β-Si<sub>3-x</sub>Al<sub>x</sub>O<sub>x</sub>N<sub>4-x</sub> by performing NMR in a higher magnetic field, 11.7 T versus 23.4 T. Panel a adapted with permission from Reference 31; copyright 2017 American Chemical Society. (b) An NMR method of separating shift anisotropy: an example showing the isotropic <sup>7</sup>Li solid-state NMR spectrum of Li<sub>2</sub>MnO<sub>3</sub> obtained via separating manifold spinning sidebands based on their orders using the 2D projection magic-angle turning phase-adjusted sideband separation method. The inset at the right shows the isotropic <sup>7</sup>Li NMR resonances around 760 ppm (red arrowhead). Panel b adapted with permission from Reference 40; copyright 2012 American Chemical Society. (c) An NMR method to average out quadrupolar coupling effects: an example showing the <sup>17</sup>O multiple-quantum magic-angle spinning (MQMAS) NMR spectrum of <sup>17</sup>O-enriched Na<sub>2</sub>O-modified SrSiO<sub>3</sub>. The isotropic spectrum is shown as the projection of the F<sub>1</sub> dimension (y-axis). The 1D spectra at the left of the isotropic spectrum are cross sections obtained from the 2D MQMAS spectrum at each isotropic resonance position indicated with dashed lines. The <sup>17</sup>O NMR spectrum on top of the 2D MQMAS shows a conventional 1D magic-angle-spinning (MAS) spectrum of very poor resolution due to residual quadrupolar coupling effects. Panel c adapted with permission from Reference 119; copyright 2016 Royal Society of Chemistry.

the acquisition time from  $t_2$  to  $t_2 - t_1$  and thus converts the MAT to PASS such that PASS spectra can be acquired with just a few  $t_1$  increments without the nuisance of nonlinear pulse timing (40). Adapting the same idea to the small flip-angle MAT pulse sequence makes pjMATPASS a robust method for application to paramagnetic materials at high fields. **Figure 2b** illustrates the separation of SSBs in two dimensions with just 32  $t_1$  increments along the indirect frequency dimension ( $F_1$ ). The center band can be identified from the slice at  $F_1 = 0$ , from which the isotropic shifts can be measured. Furthermore, shearing the 2D spectrum along the direct frequency dimension ( $F_2$ ) in conjunction with summation of all 32 slices gives rise to a quantitative isotropic spectrum of high signal-to-noise ratio as shown at the top of **Figure 2b**. The pjMATPASS pulse sequence enables the identification of isotropic resonances and the quantification of sites of different local environments with confidence (44–47). Practical discussions concerning the implementation of this method for ultrawide spectra of paramagnetic systems can be found in References 1 and 40; this situation may arise with, for example, (a) residual SSBs, (b) large  $C_Q$ , (c) short  $T_2$ , and (d) low projection pulse efficiency. The other major issue for acquiring wide-line NMR of paramagnetic samples is finite pulse bandwidth due to limited radio frequency (RF) field strengths. Frequency-sweep (i.e., chirp) pulses were introduced to tackle this problem. Recently, frequency-sweep refocusing pulses in the adiabatic regime have been successfully used in 1D acquisitions (48), relaxation measurements (49), and even MAT experiments (50).

In summary, acquiring high-resolution NMR spectra of complex materials including paramagnetic samples and structures with large quadrupolar broadening has become progressively tractable thanks to the NMR hardware and pulse developments discussed above.

### 3. EMBRACING STRONGER SIGNALS

NMR is a nondestructive isotope-specific spectroscopic technique that assesses the structures and dynamics of analytes at the atomic level. However, the Zeeman interaction is relatively small compared to thermal energy, even in a strong magnetic field. This leads to low absolute nuclear spin polarization and renders NMR insensitive, hence requiring lengthy measurements and/or large sample quantities. The limited sensitivity becomes more serious when the nucleus of interest has a low natural abundance (%), low magnetogyric ratio ( $\gamma$ ), long longitudinal relaxation time ( $T_1$ ), large quadrupolar moment, dilute concentration in the sample (e.g., a dopant), and/or wide distribution of chemical shifts. Since spin polarization is proportional to the external magnetic field and inversely proportional to temperature, acquiring NMR spectra at lower temperatures (51) and/or at higher magnetic fields (52) can enhance signal sensitivity. Beyond these traditional approaches, several new methods for enhancing signal strength have been developed in recent years.

Polarization transfer is a felicitous solution to low sensitivity in MAS NMR experiments. Polarization transfer (53, 54) from a spin system  $I$  (high  $\gamma$ ), e.g.,  $^1\text{H}$ , to a spin system  $S$  (low  $\gamma$  and/or long  $T_1$ ), e.g.,  $^{13}\text{C}$ , via dipolar coupling has been used in materials research to boost sensitivity and identify spatial relationships (55, 56). In cross-polarization (CP) experiments, the magnetization of the two different nuclei is spin-locked in their rotating frames, which allows polarization to transfer from  $I$  to  $S$  and effectively increase the signal of  $S$ . The recycle time of the CP experiment is restricted by the abundant high- $\gamma$   $I$ -spin relaxation time  $T_1$ , usually much shorter than the  $T_1$  of low- $\gamma$   $S$ -spin. Exchange of polarization occurs when the RF amplitudes of  $I$  ( $\nu_{1I}$ ) and  $S$  ( $\nu_{1S}$ ) match, i.e., attain the Hartmann–Hahn (HH) condition ( $\nu_{1I} = \nu_{1S}$ ). Under MAS (CPMAS), the HH condition is modified by the spinning rate ( $\nu_{1I} = \nu_{1S} + n \times \nu_r$ ;  $n = \pm 1$  or  $\pm 2$ ;  $\nu_r$  is the MAS rotation frequency) to account for the modulation of the dipolar coupling. The contact time for the exchange is largely limited by  $T_{1\rho}$  (i.e.,  $T_1$  in the rotating frame) (57). In addition, the rate of polarization transfer is proportional to the strength of the dipolar coupling, e.g., faster for a

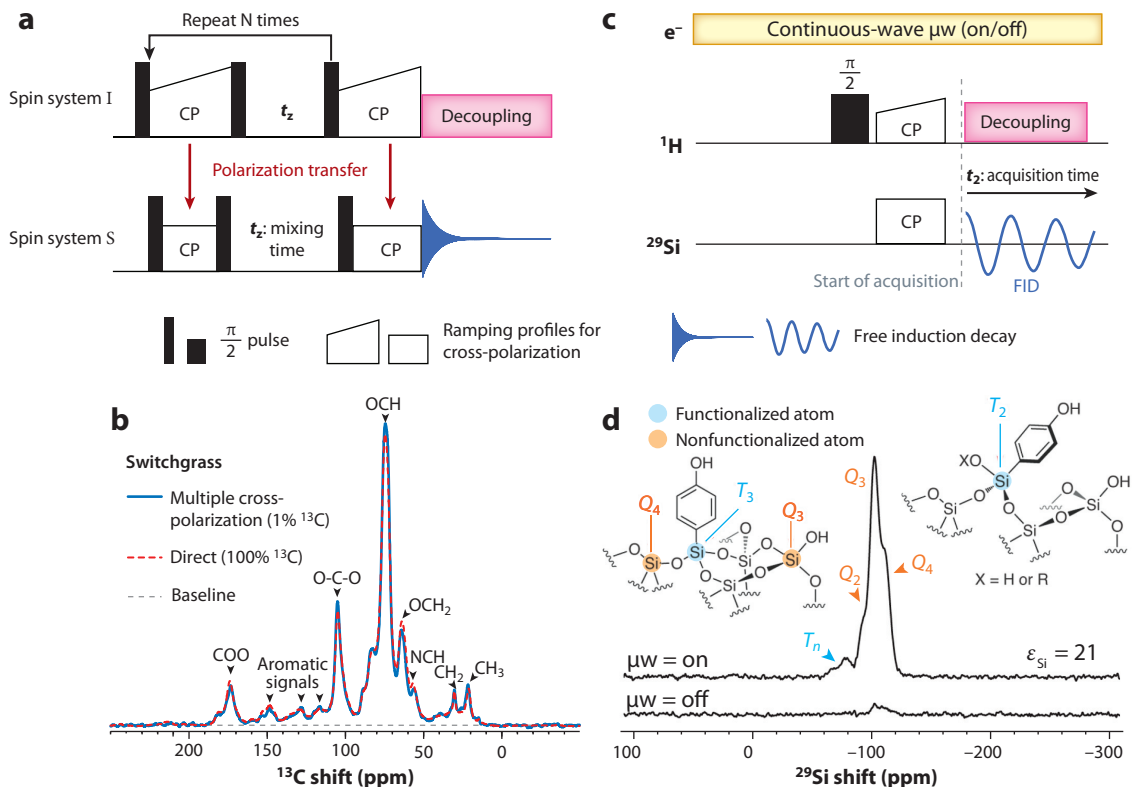


**Figure 3**

Polarization transfer for sensitivity enhancement. (a) Multiple cross-polarization (CP) pulse sequence with multiple polarization transfer steps from spin system I to spin system S. (b) CP MAS NMR spectra of switchgrass collected for equivalent time periods by direct polarization of a 100%  $^{13}\text{C}$ -enriched sample (red dashed line) versus multiple CP of a natural abundance sample with 1.1%  $^{13}\text{C}$  (blue solid line). (c)  $^1\text{H}$ - $^{29}\text{Si}$  CP pulse sequence with dynamic nuclear polarization (DNP). (d) Polarization transfer from electron spins to nuclear spins via DNP:  $^{29}\text{Si}$  MAS NMR spectra of phenol-functionalized silica collected with a conventional CP pulse sequence ( $\mu\text{w} = \text{off}$ ) and with DNP ( $\mu\text{w} = \text{on}$ ).  $\epsilon_{\text{Si}}$  is the enhancement factor of the  $^{29}\text{Si}$  NMR signal by DNP.  $T_n$  and  $Q_n$  refer to functionalized (light blue) and nonfunctionalized (orange) Si atoms, respectively, where  $n$  corresponds to the number of  $-\text{O}-\text{Si}-$  linkages off the central Si. Panel b adapted with permission from Reference 58; copyright 2014 Elsevier. Panels c and d adapted with permission from Reference 85; copyright 2011 American Chemical Society.

protonated carbon than a nonprotonated one. As a result, CPMAS experiments are in principle not quantitative in determining relative amounts of analytes, especially in the short contact time regime. The multiple CP (58) pulse sequence shown in **Figure 3a** restores the partial loss of magnetization due to  $T_{1\rho}$  relaxation during the contact time. Repeating several blocks of CP that are separated by  $t_z$ , a period of time to restore bulk magnetization, helps to retain the quantitative NMR signals as shown in **Figure 3b**.

CPMAS often is also employed to establish heteronuclear correlations (HETCORs). HETCOR spectroscopy produces a 2D map of spatial relations between two different nuclei, mediated by the dipolar coupling interaction. For quadrupolar nuclei, strong spin-lock pulses can induce leakage from the CT to other transitions when frequency crossings occur under MAS (59), compromising the spin-lock and, hence, CP efficiency. Therefore, weak RF fields and the double-quantum HH condition are preferred under fast MAS (e.g., 60 kHz) as illustrated in the

investigation of  $^1\text{H}$ – $^{27}\text{Al}$  spatial proximity (55). Alternative NMR pulse sequences have been developed to avoid the spin-lock problem with quadrupolar nuclei. Phase-shifted recoupling effects a smooth transfer of order (PRESTO) leverages the through-bond J-coupling interaction to mediate polarization transfer (60). This is known as an insensitive nuclei enhanced by polarization transfer-type experiment due to its J-coupling, rather than dipolar coupling, mechanism. In a PRESTO experiment, only one or two short pulses are applied to the quadrupolar nuclei (60).

Indirect detection of insensitive low- $\gamma$  nuclei via high- $\gamma$  nuclei, such as protons, is another useful method. In solution NMR of proteins and dilute organic molecules,  $^1\text{H}$  detection is almost exclusively used to acquire  $^{13}\text{C}$  and  $^{15}\text{N}$  signals in multidimensional experiments. In solids, the  $^1\text{H}$  linewidth is severely broadened by  $^1\text{H}$ – $^1\text{H}$  dipolar coupling, precluding an analogous implementation because the gain in signal sensitivity using indirect acquisition over direct acquisition of the nonproton spin  $X$  scales approximately according to  $\sqrt{\frac{W_X}{W_H}} * \left(\frac{\gamma_H}{\gamma_X}\right)^{\frac{3}{2}} * \frac{N_H}{N_X}$  (where  $W$  is the linewidth and  $N$  is the natural abundance) (61).  $^1\text{H}$  detection in solid-state NMR is thus a promising technique when the linewidth of the  $^1\text{H}$  spectrum can be significantly reduced. For example, Pruski and colleagues (62) have demonstrated an order of magnitude faster acquisition of indirect  $^{13}\text{C}$ – $^1\text{H}$  than of direct  $^1\text{H}$ – $^{13}\text{C}$  HETCOR with fast MAS ( $>40$  kHz), which effectively reduces the  $^1\text{H}$  NMR spectral linewidth. For indirectly detecting quadrupolar nuclei, the dipolar-based heteronuclear multiple-quantum correlation (HMQC) is most commonly used (63, 64). Recently, Rossini and colleagues (65) applied the band-selective optimized flip-angle short-transient technique (66) developed for HMQC in liquid-state NMR to solids. The rapid acquisition enabled them to acquire 2D  $^1\text{H}$ -detected HMQC of quadrupolar nuclei with acquisition times typical of those required for a 1D spectrum (65).

Another challenge in the acquisition of solid-state NMR spectra involves signals that spread out over a broad frequency range due to large quadrupolar couplings and/or shift anisotropy (see Section 2). The wide lines lead to low sensitivity. In most cases, the signal-to-noise ratio can be dramatically enhanced with a Carr–Purcell–Meiboom–Gill (CPMG) sequence with repeated pulses refocusing the transverse magnetization to form a train of spin echoes (67). CPMG pulse sequences have been applied extensively to low-sensitivity nuclei (48) with large quadrupole moments, low magnetogyric ratios, and/or low natural abundances. The echo-train signals split the normal line shape into a manifold of sidebands that trace out the powder line shape, in analogy to the signal-to-noise enhancement from MAS. The efficacy of CPMG depends on the coherence lifetime ( $T_2$ ). It has been shown recently that low-power refocusing pulses selectively excite the CT and prevent coherence loss to STs, thus extending the  $T_2$  time by, e.g., a factor of 260 for  $^{17}\text{O}$  in quartz (68). Concurrently, CPMG has been incorporated into other experiments for enhancing signal sensitivity (*a*) in high-resolution measurements such as MQMAS (69) (see Section 2), (*b*) in experiments probing spatially related spins such as rotational-echo double-resonance (REDOR) (70) (see Section 4), and (*c*) in methods designed for the acquisition of broad line shapes, including MATPASS (71) (see Section 2), broadband adiabatic inversion pulses for cross-polarization (72), and wideband, uniform rate, smooth truncation pulses (73). Detailed practical aspects of acquiring CPMG spectra can be found in Reference 67.

The most dramatic way of enhancing NMR signals is to increase the nuclear spin polarization beyond its Boltzmann thermal distribution in a process also known as hyperpolarization (74, 75). Among all mechanisms that can generate hyperpolarization, listed here are a few main methods that have been used for practical NMR applications in solids: optical pumping (76), parahydrogen-induced polarization (77), and dynamic nuclear polarization (DNP). By far the most significant advance in polarization enhancement is DNP in terms of both technology and



application development to solid-state NMR. The rest of this section focuses on the phenomenon, hardware, and applications of DNP.

First proposed by Overhauser (78) and verified by Carver & Slichter (79), DNP enhances nuclear polarization by transfer from conducting electrons in metals (**Figure 3c**), which have a magnetogyric ratio that is  $\sim 660$  times higher than  $^1\text{H}$ . Unpaired electrons of stable radical species are more often used by mixing the species with the analyte in a liquid and freezing the sample into a solid suspension before DNP experiments. For solid-state materials, this impregnation process should dissolve the radical molecule but not the analyte of interest (80). The mechanism of polarization transfer depends on the nature of the electrons and radicals (81). In addition to the Overhauser effect for the first DNP observation, the so-called solid effect is often the dominating mechanism for radicals with narrow resonances when the microwave irradiation satisfies the zero  $\omega_{\mu\text{w}} = \omega_{\text{e}} - \omega_{\text{O}}$  or double  $\omega_{\mu\text{w}} = \omega_{\text{e}} + \omega_{\text{O}}$  quantum transition conditions, wherein  $\omega_{\mu\text{w}}$ ,  $\omega_{\text{e}}$ , and  $\omega_{\text{O}}$  are the microwave, electron, and nuclear Larmor frequencies, respectively. The two conditions give opposite signs for the signal enhancement. The so-called cross effect is relevant with biradicals, e.g., nitroxides. The cross effect occurs when the difference between the two electron transition frequencies ( $\omega_{\text{e}_1}$ ,  $\omega_{\text{e}_2}$ ) matches the nuclear Larmor frequency, i.e.,  $|\omega_{\text{e}_1} - \omega_{\text{e}_2}| = \omega_{\text{O}}$ , such that polarization transfer is possible among the three spins (two electron spins and one nuclear spin). Various biradicals have been developed for cross-effect DNP. Currently, AmuPol (82) and TekPol (83) are the two most commonly used biradicals in aqueous and organic solvents, respectively. As DNP is performed at low temperature ( $\sim 100$  K), the prevention of radical crystallization in the solvent is essential. Experimentally, this is achieved by mixing radicals with a glass-forming solvent. The commonly used mixture of  $\text{d}_8$ -glycerol/ $\text{D}_2\text{O}/\text{H}_2\text{O}$  (v/v/v 60/30/10) has earned the nickname “DNP juice” (2). Freezing the sample containing the analyte and the dissolved radical forms glass that slows down the electron relaxation  $T_{1\text{e}}$  and thus enables higher DNP enhancement. Ideally, the glass formation also distributes the radicals evenly to avoid aggregation (2, 75). Nuclear spin diffusion, i.e., the diffusion of magnetization or transfer of polarization between adjacent spins via through-space dipole–dipole interactions, plays an important role in DNP (2). As the radical species is external to the solid analyte particles in the frozen suspension, polarization transfer initially occurs from the unpaired electrons to, e.g., protons on the analyte surface. Spin diffusion transfers the enhanced polarization of protons near the surface to spins in the bulk sample. Note that the interfacial protons near the radicals are often not observable due to strong interactions with the electrons that lead to rapid relaxation, a process known as bleaching. The dipolar-based spin diffusion mechanism allows for a large enhancement in the majority of nuclei in the bulk, well beyond the immediate vicinity of the radicals, particularly when the sample particle size is within the range of spin diffusion of the polarized surface species. Using repeated CP and spin diffusion, this method has been extended recently to proton-free bulk materials to enhance  $^{113}\text{Cd}$  NMR signals (84). With careful sample preparation, signal enhancement up to two orders of magnitude can be obtained, which lifts the sensitivity limitation and dramatically expands the range of systems amenable to solid-state NMR characterization (75).

DNP is naturally well suited to studying surfaces. Radical agents can be placed close to the surface, and the DNP enhancement selectively affects sites on and near the surfaces. This manifestation is known as DNP surface-enhanced NMR spectroscopy (DNP SENS) (80). DNP SENS has been employed in the investigation of organosilicates, porous materials, metal oxides, and active pharmaceutical ingredients (2). By way of example, **Figure 3d** (85) shows that  $^{29}\text{Si}$  (with a natural abundance of 4.683%) signals of nonfunctionalized Si sites ( $Q_n$ , where  $n$  is the number of  $-\text{O}-\text{Si}-$  linkages) and dilute functionalized Si sites ( $T_n$ ) can be identified within only 35 min with DNP SENS in an organic–silica hybrid material. In addition, introducing paramagnetic metal

ions instead of dissolved radicals as the polarizing agent has opened up intriguing possibilities in the study of crystalline inorganic materials (86). Recently, a metallic lithium microstructure that forms at the solid–electrolyte interphase (SEI) during the operation of lithium-ion batteries was harnessed for DNP at room temperature based on the Overhauser effect, enabling selective enhancement of both organic and inorganic species within the SEI without exogenous agents (87).

In conclusion, signal enhancement by advanced pulse sequences and technological developments in DNP have improved the efficiency of solid-state NMR experiments, enabling their application to a wider range of materials for which NMR signals were too weak for studies before.

#### 4. UNDERSTANDING STRUCTURES BY CORRELATION NMR

The properties of functional materials are often determined by local structural environments. Insights into the quantity, distribution, and connectivity of the functional moieties within a structure are critical to understanding and improving materials performance. In this regard, NMR correlation spectroscopy offers unique strengths (88).

The determination of structures without long-range order, e.g., glasses, can be challenging. Since the structural/compositional modifications of glasses are governed by the ratio and distribution of the network former (e.g.,  $P_2O_5$  and  $SiO_2$ ) and the modifier (e.g.,  $Li_2O$  and  $Na_2O$ ), probing the connectivity among the two ingredients in glasses is essential (89). REDOR is an effective solid-state MAS NMR technique to access information on the spatial proximity of nuclei. REDOR measures the distance-dependent strength of dipolar couplings between nuclear spins ( $\sum_1^n r_{i-j_n}^{-6}$ , where  $r_{i-j_n}$  is the distance between the probe nucleus  $i$  and neighboring spins  $j_n$ ) (88, 90). REDOR relies on the principles that dipolar coupling, which is averaged under MAS, can be reintroduced by applying  $180^\circ$  (or  $\pi$ ) pulses. By comparing two measurements, with and without the  $180^\circ$  recoupling pulses, the difference in signal intensity related to the strength of the dipolar coupling can be measured. Taking the ratio of the difference to the original signal excludes all other factors including the  $T_2$  relaxation and results in a so-call REDOR curve dependent only on the dipolar coupling. Analysis of the dipolar dephasing curve then yields quantitative dipolar coupling constants and, thus, internuclear distances. Practical examples have been demonstrated on glass (91) and glass-ceramics (92) to track, e.g., the  $Si^{(m)}-O-P^{(n)}$  connection with respect to their coordination number ( $m, n$ ). REDOR experiments combined with multispin simulations can probe distributions of moieties of interest, for instance, the citrate distribution at the interface of collagen and apatite in bone (93). In another example, displayed in **Figure 4a**, Reimer and coworkers (94) employed  $^{13}C\{^{15}N\}$  REDOR to map out the possible distribution scenarios (large cluster, small cluster, random, or alternating) of an organic linker (1,4-benzenedicarboxylate) with two different functional groups ( $-NH_2$  and  $-CH_3$ ) in MOF-5, illustrating why a certain combination of functional groups results in optimal selectivity for  $CO_{2(g)}$  adsorption.

In REDOR experiments, signals from naturally abundant  $j$  spins that are not coupled to  $i$  spins may interfere with the measurements of heteronuclear  $i-j$  dipolar coupling (95). To address this issue, transferred-echo double-resonance (TEDOR) (95) can be used, in which the recoupling  $180^\circ$  pulses (see above) are applied before/after the transfer of coherence by simultaneous  $90^\circ$  pulses on both nuclei. An example of  $^7Li\{^{19}F\}$  TEDOR by Bodart et al. (96) demonstrated the estimation of the Li–F interatomic distance in montmorillonite, which was used to determine the possible location (hexahedral or octahedral) of lithium ions and their migration path. There are several variants of REDOR-type experiments when the spin pairs involve quadrupole nuclei. Early transfer of populations in double resonance (TRAPDOR) uses continuous-wave irradiation for recoupling (97). Such an experiment is robust and simple, but its result of dipolar dephasing depends on quadrupole coupling and RF parameters in addition to the dipolar coupling constant,

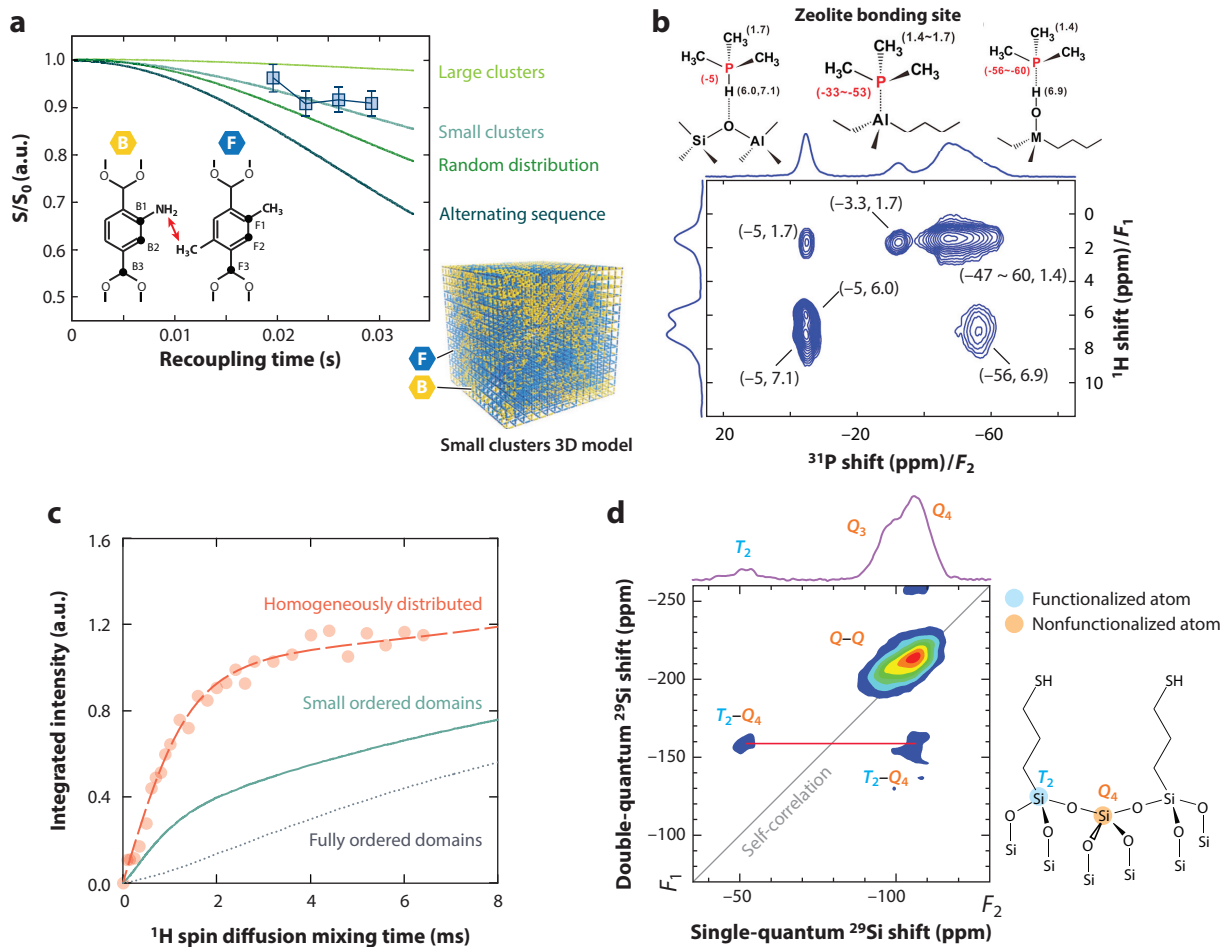


**Figure 4**

Structural elucidation through nuclear magnetic resonance (NMR) correlation spectroscopy. (a) Rotational-echo double-resonance (REDOR) NMR: illustration of the use of  $^{13}\text{C}\{^{15}\text{N}\}$  REDOR to probe heterogeneity of mixed organic linkers in metal-organic frameworks (MOFs) by comparing the experimental  $^{13}\text{C}\{^{15}\text{N}\}$  REDOR decay (blue squares) with calculated REDOR decay curves (green solid lines) based on models with the linkers apportioned into large clusters, small clusters (inset 3D model), a random distribution, or an alternating sequence. B and F are labeling molecules attached to different organic linkers, which serve as distance probes. Panel a adapted with permission from Reference 94; copyright 2013 American Association for the Advancement of Science. (b) Heteronuclear correlation (HETCOR) spectroscopy: application of  $^1\text{H}$ - $^{31}\text{P}$  HETCOR for distinguishing the bonding acid sites of an HY zeolite. Numbers in parentheses indicate 2D coordinates of the resonances. Trimethylphosphine was used as a probe molecule due to the sensitivity of its  $^1\text{H}$  and  $^{31}\text{P}$  chemical shifts to the nature of the zeolite bonding site (structures shown at top, with the range of chemical shifts shown in red in parentheses). Panel b adapted with permission from Reference 3; copyright 2018 American Chemical Society. (c) Spin diffusion NMR: This example uses  $^1\text{H}$ - $^1\text{H}$  radio frequency-driven recoupling spin diffusion correlation spectroscopy to examine the distribution of biphenyl dicarboxylic acid and bipyridyl dicarboxylic acid mixed linkers in the MOF known as DUT-5. The experimental data points are represented by circles, and the curves are based on models with linkers that are homogeneously distributed (orange dashed line), in small ordered domains (blue solid line), and in fully ordered domains (purple dotted line). Panel c adapted with permission from Reference 109; copyright 2015 Wiley-VCH. (d) Illustration of the use of 2D  $^{29}\text{Si}$ - $^{29}\text{Si}$  double-quantum/single-quantum NMR to determine the connectivity of Si-O-Si and Si-O(H)-alkyl linkages. The horizontal red line connects resonances suggesting correlation between  $Q_4$  and  $T_2$ .  $T_n$  and  $Q_n$  refer to functionalized and nonfunctionalized Si atoms, respectively, where  $n$  corresponds to the number of -O-Si- linkages off the central Si (structure shown at right). Panel d adapted with permission from Reference 162; copyright 2017 Royal Society of Chemistry.

and a quantitative analysis usually requires a full spin simulation. In comparison, rotation-echo adiabatic passage double resonance (REAPDOR) (98) and rotation-echo saturation double resonance (RESPDOR) (99, 100) can lead to universal REDOR curves that can be fitted with dipolar coupling constants only.

In addition to their role in signal enhancement (see Section 3), HETCOR experiments are often used to elucidate the proximity of X and Y spins. The relative spatial proximity of different components can be estimated. When protons are involved, HETCOR is performed in conjunction with  $^1\text{H}$ - $^1\text{H}$  homonuclear decoupling for enhanced resolution to differentiate individual  $^1\text{H}$  species. Significant work has been carried out using HETCOR on polymers or polymer-mineral composite systems (11). Rankin et al. (101) demonstrated that the surface  $Q_n$  species on silica-alumina catalysts can be established through CP methods with  $^1\text{H}$ - $^{29}\text{Si}$  HETCOR (102, 103).

HETCOR experiments have also been widely applied in the study of zeolite solid acid catalysts (104). Catalytic reactions in zeolitic frameworks rely on the concentration and distribution of accessible active sites, i.e., Lewis acid and Brønsted acid sites, which represent extraframework six- and five-coordinate Al or framework four-coordinate Al, respectively (103). Accordingly, quantitative investigation of the acid site identity and distribution is key to optimizing catalytic performance.  $^1\text{H}$ - $^{27}\text{Al}$ ,  $^1\text{H}$ - $^{29}\text{Si}$ , and  $^{29}\text{Si}$ - $^{27}\text{Al}$  correlation experiments have been successfully applied to study the Si-O(H)-Al connectivity in aluminosilicates (105). The sensitivity of  $^{31}\text{P}$  shifts in trimethylphosphine (103) to acidity enables this organic molecule to directly probe the nature of Lewis and Brønsted acid sites with regards to their spatial distribution over the Si-O(H)-Al linkages. As shown in **Figure 4b** (3), the pairs of  $^1\text{H}$  and  $^{31}\text{P}$  chemical shifts of trimethylphosphine from  $^1\text{H}$ - $^{31}\text{P}$  HETCOR can be used to identify the corresponding coordination models that are characteristic of certain Al species. These structural insights may be correlated with and verified by density functional theory calculations and practical catalytic reactions to trace the origin of high performance.

REDOR and HETCOR NMR techniques probe atomic distances up to one nanometer. To extend the length scale in probing spatial proximity, researchers may take advantage of  $^1\text{H}$  spin diffusion. This approach is particularly effective for measuring  $^1\text{H}$ - $^1\text{H}$  interatomic distances due to the high abundance and high  $\gamma$  of  $^1\text{H}$ ; dipolar coupling strength ( $D_{ij}$ ) scales with  $\gamma^2(D_{ij} = -\frac{\gamma_i\gamma_j}{8\pi^2r^3}(3\cos^2\theta(t) - 1))$ . Under fast MAS, anisotropic interactions including dipole-dipole couplings are attenuated. Therefore,  $^1\text{H}$  spin diffusion measurements are often facilitated by radio frequency-driven recoupling (RFDR) (106) with rotor-synchronized  $180^\circ$  pulses that recouple the dipolar couplings. In 2D correlation NMR, the growth of correlation peaks (off-diagonal signals) as a function of mixing time ( $\tau_m$ ) reveals the distance-dependent homonuclear dipolar coupling strength among  $^1\text{H}$  spins from different moieties. Faster growth of the correlation peaks (stronger signals) corresponds to closer proximity. Substantial work with this method has been performed by the Schmidt-Rohr group (107, 108). Another example of the  $^1\text{H}$  spin diffusion method was demonstrated by Krajnc et al. (109) (**Figure 4c**), who showed that  $^1\text{H}$  spin diffusion curves can be used to distinguish between different spatial distributions of organic linkers in a mixed-ligand Al-MOF through a series of measurements and calculations on different model structures. More recently, the same group developed a  $^{13}\text{C}$ -detected  $^1\text{H}$  diffusion pulse sequence ( $^1\text{H}$  RFDR followed by  $^1\text{H}$ - $^{13}\text{C}$  CP) to achieve the same goal, but with higher contour resolution offered by  $^{13}\text{C}$  NMR (110). This method helped to clarify correlation peaks that had been blurred previously due to insufficient  $^1\text{H}$  NMR spectral resolution.

In addition to  $^1\text{H}$  spin diffusion experiments, homonuclear correlations can be established by multiple-quantum experiments (111). Multiple adjacent spins of the same kind can produce quantum coherence beyond the first order. Among techniques exploiting this phenomenon, double-quantum experiments (112) are the most common due to the relatively high yield of

double-quantum coherence compared with other higher orders. A recent example by Kobayashi et al. (113) employed DNP-enhanced (see above)  $^{29}\text{Si}$ – $^{29}\text{Si}$  double-quantum/single-quantum correlations, in which the homonuclear dipolar recoupling is achieved by exciting double-quantum coherences with the supercycled POST-C5 sequence (114) to resolve the connectivity between  $T_n$  or  $Q_n$  sites anchoring on silica nanoparticles (**Figure 4d**). The narrow line width of  $^{29}\text{Si}$  resonances and sensitivity enhancement via DNP are combined in this method to identify changes in relative positions of local Si coordination arising from different synthetic conditions (115). Multiple-quantum spin-counting experiments can be used to determine the size of spin clusters based on the relative intensity of excited quantum coherences of different orders (116). These experiments are more practical for nuclear spins with high magnetogyric ratios and natural abundance such as  $^1\text{H}$ ,  $^{19}\text{F}$ , and  $^{31}\text{P}$  because the generation of high-order quantum coherence requires strong homonuclear dipolar couplings.

In brief, many solid-state NMR techniques have been developed for elucidating structures by establishing spin correlations. The majority of these methods, such as CP-based techniques, involve  $^1\text{H}$  spins, which are not common constituents in inorganic compounds.  $^{19}\text{F}$  spins are similarly useful when present. Only a few of the most common methods for materials research are discussed here, covering a small fraction of the vast library of NMR correlation techniques.

## 5. PROBING ION DYNAMICS

Local rotational motion, long-range diffusional motion, and ion exchange are relevant to a wide variety of structural and functional materials. Rotational motion of the structural framework is often critical to concerted ion transport in biological and technological systems, such as ion conduction across cell membranes (117). Diffusional motion is essential for many applications, such as fast ion conductors used in energy conversion and storage systems and sensors (118), while it can be detrimental for others, such as hydrogen embrittlement of steel.

Molecular motion affects NMR interactions including chemical shifts, CSA, dipolar coupling, and quadrupolar coupling and is often the main mechanism for nuclear relaxation. In solid state, motion-induced effects manifest as changes in NMR line shapes, averaged chemical shifts, reduced dipolar/quadrupolar couplings, and temperature-dependent behavior that can be investigated with numerous NMR methods. As ion dynamics strongly depend on atomic structure, the correlations of ion dynamics and structure can be established to guide new materials design. In this section, we review practical examples that employ NMR spectral line shape analysis, 2D NMR, relaxometry, and PFG NMR to assess ion dynamics.

Monitoring changes in NMR spectral linewidth to study ion dynamics is a commonly employed method. In solid-state NMR, the resonances are broadened by NMR interactions such as shift anisotropy, dipolar, and quadrupolar couplings. Fast ion dynamics at elevated temperatures typically result in a reduction of these NMR interactions and narrowing of the NMR resonances. The effect of motion-induced narrowing is well illustrated in the evolution of variable-temperature  $^{23}\text{Na}$  and  $^{17}\text{O}$  spectra of  $\text{Na}_2\text{O}$ -modified  $\text{SrSiO}_3$ , which was developed for potential application as a solid electrolyte in solid-oxide fuel cells. As demonstrated in Reference 119, significant narrowing of the  $^{23}\text{Na}$  NMR resonance with increasing temperature is observed, while the  $^{17}\text{O}$  NMR resonances are invariant. These observations suggest enhanced  $\text{Na}^+$  motion with temperature and very little movement of  $\text{O}^{2-}$ . Therefore,  $\text{Na}^+$  rather than  $\text{O}^{2-}$  contributes to the high ionic conductivity measured with impedance spectroscopy. It is worth mentioning that the crystallization of  $\text{Na}_2\text{O}$ -modified  $\text{SrSiO}_3$  above  $500^\circ\text{C}$  attenuates  $\text{Na}^+$  conduction, which results in broadening of the  $^{23}\text{Na}$  NMR linewidth. The correlation time ( $\tau$ ) and activation energy ( $E_a$ ) of ionic motion can often be extracted from analysis of the line narrowing of the central

NMR transition ( $1/2 \leftrightarrow -1/2$ ) with temperature (120, 121). As an example of the utility of these methods, Forse et al. (122) analyzed  $^1\text{H}$  and  $^{19}\text{F}$  NMR linewidths to shed light on the diffusion mechanisms of cations and anions of ionic liquid electrolytes in supercapacitors, as a function of temperature, solvent additives, and electric potential.

Self-diffusion ( $D$ ) in superionic solids or liquids within porous materials can be probed with PFG NMR (123). With this technique, the normalized attenuation of the transverse magnetization intensity ( $\frac{I}{I_0}$ ) due to ionic/molecular diffusion for a nucleus with magnetogyric ratio  $\gamma$  is recorded as a function of the diffusion time ( $\Delta$ ) or the magnitude of the gradient field (manipulated by the gradient pulse duration,  $\delta$ , and the amplitude of the gradient pulse,  $g$ ) (**Figure 5a, i**). Fast dephasing correlates with rapid diffusion according to  $\frac{I}{I_0} = \exp[-g^2\gamma^2\delta^2(\Delta - \frac{\delta}{3}D)]$ . There are several approaches to measure diffusion with PFG NMR; the appropriate choice will depend on the  $T_1$  and  $T_2$  relaxation behavior of the materials systems of interest and whether the material is electronically conductive because eddy currents can be induced in the sample and must be accounted for with an appropriate delay period.

The measurement of diffusion coefficients with PFG NMR is limited to relatively fast ionic motion in solids, typically at least  $10^{-13} \text{ m}^2 \text{ s}^{-1}$ , though the bounds depend on the hardware (accessible gradient magnitudes) and the sample (primarily relaxation, which can limit gradient and diffusion times). MAS PFG NMR can reduce the rate of relaxation mediated by anisotropic couplings (4) and thus offers an opportunity to set longer  $\delta$  and  $\Delta$  than conventional static PFG NMR for the accurate determination of diffusivity. An additional benefit of MAS is improved spectral resolution, which may enable more specific determination of the component that undergoes long-range diffusion. Kärger et al. (4) demonstrated the benefits of MAS in PFG NMR for mesoporous silica KIT-6 by showing that the signal attenuation corresponds to the fast exchange between resolved acidic protons and  $^1\text{H}$  in water molecules. Through postacquisition conversion of gradient fields to wave vectors ( $q$ ;  $q = \gamma \cdot \delta \cdot g$  in the unit of  $\text{length}^{-1}$ ), the signal attenuation can be examined with respect to  $q$ . The wave vector here is analogous to the wave vector in X-ray diffraction. The diffraction-like peaks in PFG NMR arise from restrictive features such as grain boundaries of the host matrices of the diffusing ions (124). This is clearly illustrated in **Figure 5a, ii** (125) by comparing a polycrystalline solid electrolyte to a single crystal sample. Polycrystalline  $\text{Li}_{6.5}\text{La}_3\text{Zr}_{1.5}\text{Ta}_{0.5}\text{O}_{12}$  exhibits numerous  $^7\text{Li}^+$  diffraction peaks as lithium diffuses within the crushed powder and reaches grain boundaries, while a single crystal of the same composition shows few to no diffraction-like features.

NMR relaxometry encompasses several different techniques to access ion dynamics. Depending on the timescale of the ion dynamics (**Figure 5b**) (126),  $T_1$ ,  $T_{1\rho}$ , and  $T_2$  relaxation times (127) as well as spin-alignment echo (SAE) measurements (126) can be employed. NMR relaxation is driven by the fluctuation of the local magnetic field at the nucleus as a consequence of ion motion. Briefly,  $T_{1\rho}$  is the longitudinal relaxation time in the rotating reference frame with spectral density near the RF field strength 10–100 kHz and thus is sensitive to  $10^{-5}$  s timescales as opposed to  $T_1$  in the laboratory reference frame that is more sensitive to  $10^{-8}$  s, the inverse of Larmor frequency ( $\omega_0$ ) timescales.  $T_1$  and  $T_{1\rho}$  measurements can yield information on both short-range hopping ( $\omega_0\tau_0 \gg 1$ ) and long-range diffusion ( $\omega_0\tau_0 \ll 1$ ) (127). Specifically, the turning point at  $T_1$  minimum where  $\omega_0\tau_0 \approx 1$ , when the longitudinal relaxation rate [ $R_{1(\rho)} = T_{1(\rho)}^{-1}$ ] is at its maximum, reflects the mean jump rate [ $\tau(T)$ ] in the diffusion process (**Figure 5d**). As can be seen in **Figure 5d** (128), the cusp of the  $^7\text{Li}$  NMR relaxation rate migrates toward lower temperatures when ion dynamics are enhanced in lithium-ion solid electrolytes, consistent with increasing ionic conductivities observed by impedance spectroscopy (128). NMR relaxometry can also provide insights on the mechanism by which subtle changes in atomic structure can have disproportionate impacts on ionic conductivity (129, 130). SAE NMR is often used to access

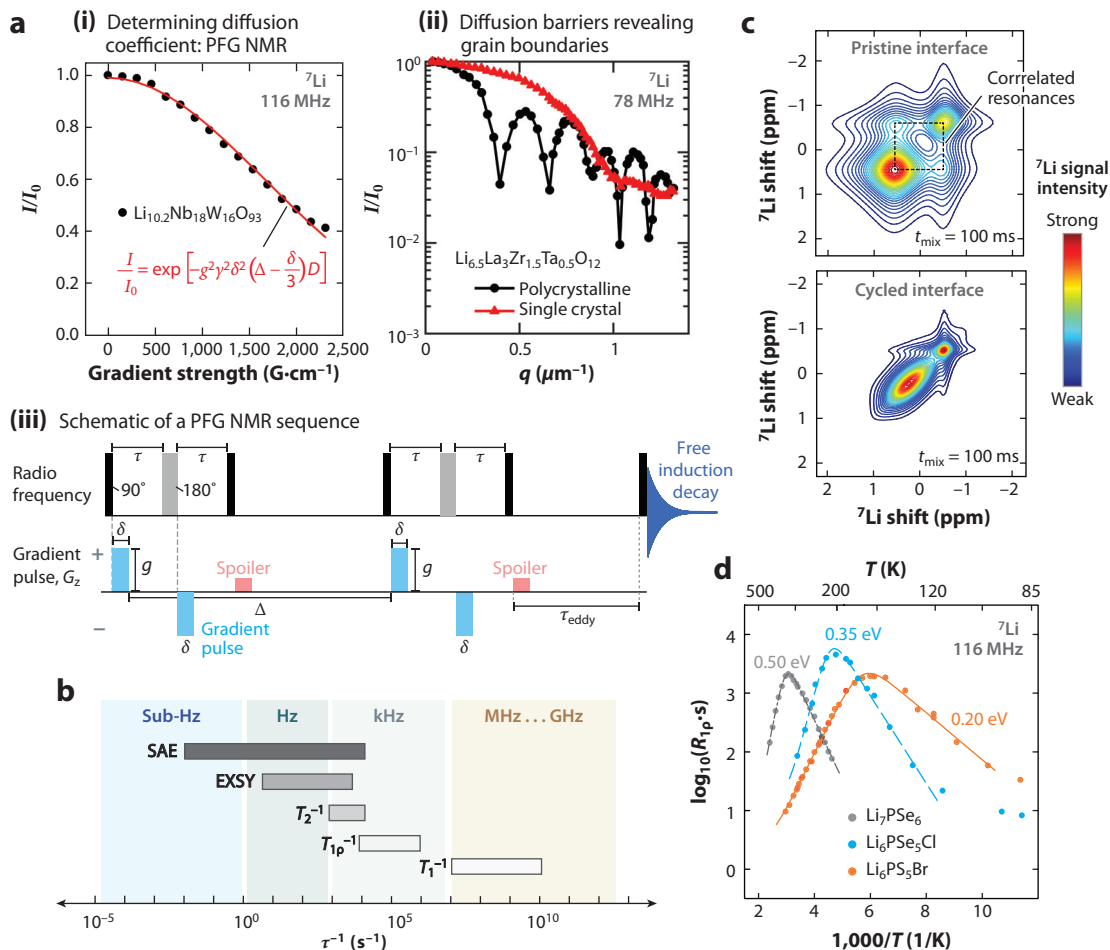


**Figure 5**

NMR measurements of ion dynamics. (a) PFG NMR for probing ion diffusion: a  $^{7}\text{Li}$  PFG NMR decay curve of  $\text{Li}_{10.2}\text{Nb}_{18}\text{W}_{16}\text{O}_{93}$ , fitted to the equation to extract the diffusivity  $D$  ( $i$ ) and a schematic of a PFG NMR sequence (iii).  $G_z$  is the gradient pulse along the  $z$ -axis,  $\tau$  is the interpulse delay,  $\delta$  is the duration of the gradient pulse,  $g$  is the amplitude of the gradient pulse,  $\Delta$  is the diffusion time, and  $\tau_{\text{eddy}}$  is the period to dissipate the gradient-induced eddy current before data acquisition. Spoiler refers to the spoiling gradient to remove the unwanted transverse coherences before the start of subsequent RF pulsing. Subpanel *i* adapted with permission from Reference 163; copyright 2018 Nature Springer. (ii) Grain boundary versus bulk diffusion in  $\text{Li}_{6.5}\text{La}_3\text{Zr}_{1.5}\text{Ta}_{0.5}\text{O}_{12}$  captured by  $^{7}\text{Li}$  PFG NMR. Subpanel *ii* adapted with permission from Reference 125; copyright 2019 AIP Publishing. (b) The time scales/frequencies of ion dynamics that can be accessed with various NMR techniques.  $T_2^{-1}$  is the spin–spin relaxation rate,  $T_{1\rho}^{-1}$  is the spin–lattice relaxation rate in the rotating frame, and  $T_1^{-1}$  is the spin–lattice relaxation rate in the laboratory frame. Panel *b* adapted with permission from Reference 126; copyright 2012 Wiley-VCH. (c)  $^{7}\text{Li}$  EXSY spectra of an  $\text{Li}_6\text{PS}_5\text{Cl}$ – $\text{Li}_2\text{S}$  electrolyte–cathode composite before (top) and after (bottom) electrochemical cycling. Strong off-diagonal (cross) peak intensity (top) indicates magnetization exchange between lithium in the cathode and in the electrolyte of the pristine composite. No cross peaks are detected after cycling due to the increased electrolyte–cathode interfacial resistance. Panel *c* adapted with permission from Reference 134; copyright 2017 Nature Publishing Group. (d)  $^{7}\text{Li}$   $T_{1\rho}$  relaxation rate ( $R_{1\rho}$ ) of argyrodite solid lithium-ion electrolytes as a function of temperature and composition. Anion mixing and polarizability influence transport as evidenced by changes in the position of the relaxation rate maximum and slopes. Panel *d* adapted with permission from Reference 128; copyright 2013 American Chemical Society. Abbreviations: EXSY, exchange spectroscopy; NMR, nuclear magnetic resonance; PFG, pulsed field gradient; RF, radio frequency; SAE, spin-alignment echo.

dynamics of quadrupolar nuclei (126). Recall that the quadrupolar frequency of a nucleus at a specific site is inherent to interactions between the nuclear quadrupole moment and the EFG. Thus, depending on the local symmetry and the orientation of local charges, ion hopping between electrically nonequivalent environments causes fluctuations in the quadrupolar interaction. This leads to nuclear relaxation and decay of the echo amplitude; even the quadrupole nuclei do not move directly. SAE is then recorded with a two-time correlation function ( $S_2$ ) as a function of mixing time in SAE NMR (5). Elementary steps of ion hopping among possible sites in a given crystalline structure can be determined with SAE NMR in conjunction with complementary information acquired from  $T_1$  and/or  $T_{1\rho}$  measurements (131).

Studying ion dynamics spanning across multiple timescales requires a complementary suite of methods (**Figure 5b**) (126). As an accompaniment to the aforementioned techniques, two-dimensional exchange spectroscopy (2D-EXSY) can be used to probe chemical exchange on relatively long timescales (milliseconds to seconds). When chemical exchange occurs during the period of mixing time ( $t_m$ ) in 2D-EXSY, off-diagonal cross peaks are observed. The exchange rate can be obtained based on the evolution of the cross-peak intensity versus the autocorrelation peak intensity (along the diagonal) as a function of mixing time (132). In addition, short-range ion diffusion and ion transport pathways can be probed (133), and the spatial proximity of two different structural sites or chemical phases can be quantified (**Figure 5c**) (134).

With multifaceted NMR tools for studying ion dynamics on a variety of timescales, critical information concerning the diffusion coefficient, ion hopping pathway, ionic conductivity, correlation time, and activation energy can be obtained. Important structure–property–performance relations can be established.

## 6. IMAGING MATERIALS

In addition to local atomic structure, the performance of materials depends on their microstructure, composition gradients, and spatial distribution of dopants and charge carriers. While retaining the noninvasive, isotope-specific features of NMR, MRI provides spatial resolution of an analyte on the order of micrometers by applying magnetic field gradients. To achieve this, in addition to the constant external magnetic field ( $B_0$ ) provided by the magnet and the local magnetic field ( $B_{\text{local}}$ ) induced by the spins in analytes, an additional controlled gradient field along  $x$ ,  $y$ , and/or  $z$  directions [ $G(x, y, z, t)$ ], where  $t$  denotes time, is engineered with a set of gradient coils. Therefore, the spatial information of the analyte can be encoded into the detected NMR frequency,  $\omega = g(B_0 + B_{\text{local}} + G(x, y, z, t))$ . MRI allows the mapping of nuclear spins in space and offers both qualitative and quantitative information on local structural environments that are relevant to material performance.

MRI has been widely employed in clinical/biomedical research (135) but is still in the early stages of its application to materials research. Materials MRI faces a different set of challenges than biomedical MRI; the former is associated with image distortions induced by broadening from spin interactions other than from the applied gradient, including magnetic susceptibility. The transmission and reception of RF pulses and NMR signal can also be affected in electronically conductive samples; therefore, image distortions are particularly severe for systems containing metallic components such as electrochemical devices. Experimentally, image distortion can be minimized by aligning the conductive surface of the analyte parallel to both the  $B_1$  (RF) and  $B_0$  (magnetic) fields (135). In addition to image distortion, conductive components exhibit shorter relaxation times ( $T_1$ ,  $T_2$ , and  $T_2^*$ ;  $T_2^*$  is also called effective  $T_2$ ) than insulating materials, causing line broadening and poor spectral resolution. Efforts have been made to address these challenges. For instance, Romanenko et al. (136) demonstrated that single-point ramped imaging with  $T_1$



enhancement (SPRITE)—a method that utilizes short and low flip-angle excitation pulses and pure phase-encoding gradients—is robust against field inhomogeneity associated with magnetic susceptibility. In SPRITE, acquiring a single data point within a fixed phase-encoding time ( $t_p$ ), which is shorter than  $T_2^*$ , makes the magnetic resonance images less susceptible to distortion. Additionally, the ramped gradient circumvents the need to switch the gradient on and off between each acquisition, thus providing more efficient data collection. Therefore, SPRITE is suitable for real-time MRI studies of electrochemical cells assembled with alkali metals (136).

Performing MRI on nuclei with low natural abundance and short relaxation times is usually impractical due to the limited signal. Instead, imaging on neighboring nuclei, typically  $^1\text{H}$ , of high natural abundance and sensitivity provides indirect access to the nucleus of interest for magnetic resonance visualization. As the relaxation times are sensitive to the presence of metal ions, a general procedure starts with establishing the correlation between  $^1\text{H}$   $T_1$  (or  $T_2^*$ ) times and the concentration of metal ions such as  $\text{Li}^+$  or  $\text{Cu}^{2+}$  with standard samples. Therefore, the  $T_1$  ( $T_2^*$ )– $[\text{M}^{x+}]$  calibration curve informs the changes in  $[\text{M}^{x+}]$  spatially and temporally. One example (**Figure 6a**) involves a set of copper corrosion experiments performed by Bray et al. (137), employing MRI to track the wave front of  $\text{Cu}^{2+}$  distribution between anode and cathode. The variation of the observed  $T_1$  times of  $^1\text{H}$  at both electrodes indirectly reflects where  $\text{Cu}^{2+}$  ions accumulate and how they propagate under the passage of current. Along the same lines, Romanenko et al. (6) exploited the  $T_2^*$  response to  $\text{H}^+$  ion mobility in lithium bis(fluorosulfonyl)imide (LiFSI)-doped  $[\text{P}_{1444}^+][\text{FSI}^-]$  ionic plastic crystal electrolytes. Concentrated  $\text{Li}^+$  ions from LiFSI disrupt the crystalline domains in this system, leading to an increasing amount of amorphous phase exhibiting liquid-like  $\text{H}^+$  motion and, thus, a commensurate increase in  $T_2^*$ . Based on the derived correlation of  $^1\text{H}$   $T_2^*$  with  $[\text{Li}^+]$  concentration, the  $T_2^*$  contrast MRI revealed a nonuniform distribution of  $\text{Li}^+$  ions (6). The depletion zones hinder  $\text{Li}^+$  transport, leading to poor performance of this class of solid electrolytes.

Ilott et al. (138) turned the problematic magnetic susceptibility effects into an advantage in their recent work, wherein the susceptibility-induced difference in a magnetic-field-strength map served as a measure of the state of charge and manufacturing defects in lithium-ion batteries. As demonstrated in **Figure 6b** (138), the differences in susceptibility of  $\text{Mn}^{2+,3+,4+}$ ,  $\text{Co}^{3+,4+}$ , and  $\text{Ni}^{2+,3+}$  provide a mechanism for the magnetic field-strength map to shed light on the metal oxidation states and distribution in lithium-ion battery cathode materials. This method can be used to perform early diagnosis of battery health since inhomogeneities are often associated with manufacturing defects that could lead to device failure or safety hazards during operation.

The electrolyte diffusion coefficient and transference number, both of which influence the performance of batteries, can be deduced by mapping  $^7\text{Li}/^{19}\text{F}$  concentration profiles of dissolved  $[\text{Li}^+][\text{PF}_6^-]$  as a function of electric current densities via MRI (139). Also, microstructural lithium formation can be nondestructively probed with in situ  $^7\text{Li}$  chemical shift imaging (CSI).  $^7\text{Li}$  CSI has shown that the depletion of  $\text{Li}^+$  in the electrolyte salt, e.g.,  $\text{LiPF}_6$ , by irreversible side reactions triggers the formation of a dense mossy layer under higher current density followed by dendritic growth near the anode surface (140, 141). In the emerging field of all-solid-state batteries,  $^7\text{Li}$  CSI has also been employed to investigate the microstructural growth of lithium inside solid electrolytes, such as  $\text{Li}_{6.5}\text{La}_3\text{Zr}_{1.5}\text{Ta}_{0.5}\text{O}_{12}$  (**Figure 6d**), showing that even dense solid electrolytes do not necessarily prevent dendrite formation and the associated short circuits (142). In another example, 3D  $^7\text{Li}$  MRI was used to identify Li deficiency at an interface between Li and  $\text{Li}_{10}\text{GeP}_2\text{S}_{12}$  after cycling an all-solid-state battery (7). Such Li-deficient layers impede Li diffusion, leading to high interfacial resistance and, hence, degradation of solid-state battery performance.

The relatively low spatial resolution of MRI, on the order of micrometers, leaves MRI impotent when resolution at the molecular level is required. Magnetic resonance force microscopy (MRFM)

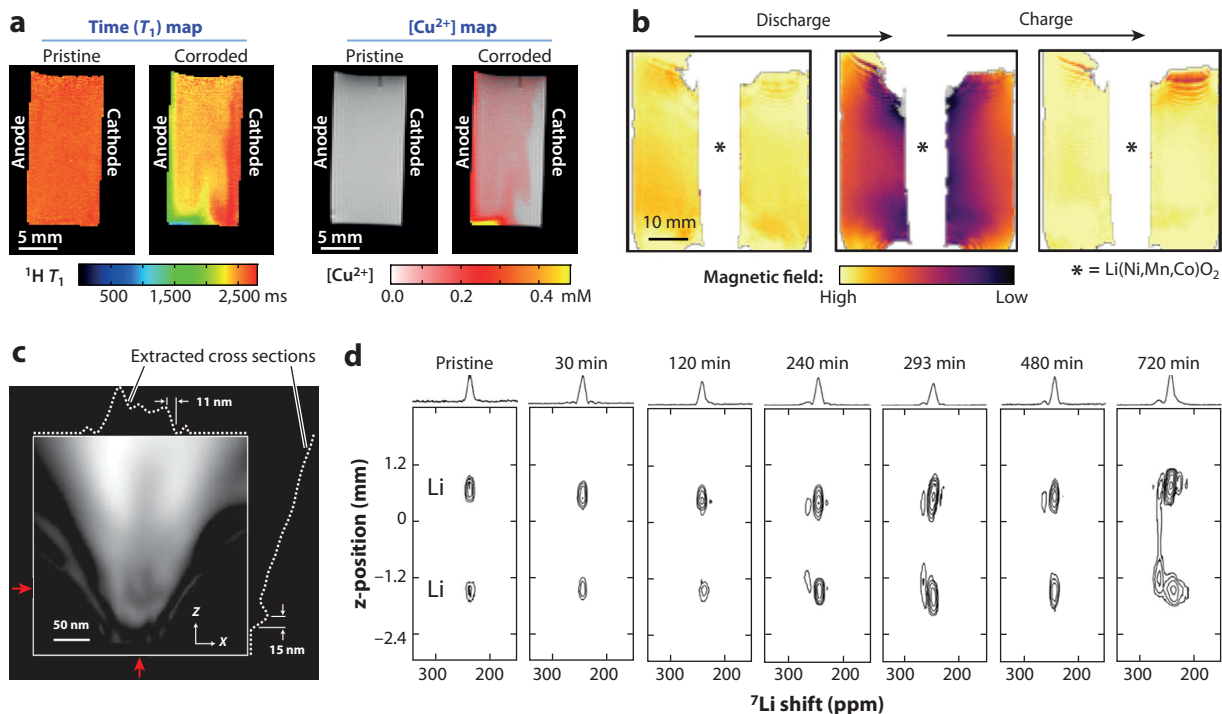


**Figure 6**

Magnetic resonance imaging (MRI). (a)  $Cu^{2+}$  dissolution in an aqueous solution probed indirectly by monitoring the  $^1H$  NMR  $T_1$  relaxation time map (left) and the corresponding derived  $[Cu^{2+}]$  distribution map (right) from a calibration curve. Panel a adapted with permission from Reference 137; copyright 2016 Wiley-VCH. (b) Probing the state of charge in an  $Li_xNi_{0.5}Mn_{0.3}Co_{0.2}O_2||$ graphite lithium-ion battery by probing the induced magnetic field with  $^1H$  MRI of water in a container that surrounds the battery cell. In this imaging geometry, the battery sits in the void [labeled  $Li(Ni,Mn,Co)O_2$ ]]. Panel b adapted with permission from Reference 165; copyright 2018 Nature Publishing Group. (c) Projected  $^1H$  density of polystyrene detected by magnetic resonance force microscopy. Cross-sectional positions are indicated by red arrows. Panel c adapted with permission from Reference 144; copyright 2013 American Physical Society. (d)  $^7Li$  chemical shift imaging of dendrite growth in an  $Li||Li$  symmetric cell through an  $Li_{6.5}La_3Zr_{1.5}Ta_{0.5}O_{12}$  solid electrolyte. Li microstructures (small shoulder next to the main Li peak at  $\sim 250$  ppm) are observed ( $>240$  min) prior to the full short circuit (720 min). Panel d adapted with permission from Reference 142; copyright 2019 American Chemical Society.

is an alternative for improved resolution to the nanometer scale (143). In MRFM, RF pulses flip the magnetic moments in analytes, inducing a weak magnetic force that acts on an atomic force microscopy cantilever (or nanowire) to which the analytes are attached. The mechanical oscillations of the cantilever, with the same frequency as that of the magnetic moments being inverted, are then optically detected by an interferometer. Signal to noise in MRFM is dictated by the usual NMR parameters such as the resonance frequency ( $\omega_0$ ) and the quality factor  $Q$ , and also by the magnetic spring constant ( $k_m$ ), which depends on the dimension of the cantilever as well as the magnetic field gradient (143). Tremendous effort has been invested in making higher-quality magnetic tips, more responsive mechanical transducers, and more efficient measurement protocols (143). Nichol et al. (144) employed nanoconstriction to concomitantly produce RF fields and magnetic field gradients, in combination with a silicon nanowire. The  $^1H$  density in polystyrene (the analyte) projected onto a 2D map can be resolved down to nearly 10 nm (Figure 6c) (144). The image resolution attained with this innovation is comparable to that of scanning electron microscopy, hence facilitating nanoMRI via MRFM. Note that the penetration depth of RF waves

used here can be much larger than that of electrons or X-rays employed in conventional microscopy methods.

To conclude, MRI has become a powerful and effective analytical probe in materials research. The aforementioned technique developments showcase the capability of MRI to study spatial and temporal distributions with high resolution and across various length scales.

## 7. NOVEL NMR PROBE AND ACCESSORY DESIGNS FOR IN SITU NMR CHARACTERIZATION UNDER NONAMBIENT CONDITIONS

Understanding physical and chemical processes that take place at extreme conditions such as high temperature and/or pressure is of great importance to the development of novel materials and their applications. For example, molecular hydrogen has been predicted to be metallic under sufficiently high pressure; however, direct experimental evidence is still needed (145). Owing to technical innovations, high-temperature and high-pressure NMR is becoming more accessible. In this vein, we briefly discuss the recent advancements in NMR hardware with a focus on the design of probes and accessories to accommodate various challenges of in situ acquisitions.

The time evolution of crystallization and catalytic processes, in which chemical reactions often occur at solid–liquid interfaces, is an important research subject and requires in situ studies. Conventional NMR rotors are not gas or moisture tight under ambient conditions, which prohibits MAS NMR with a mixture of solid and liquid components as well as in situ studies at elevated temperatures and/or pressures. These obstacles are overcome by the design of high-temperature/pressure NMR rotors (146) that use O-rings and sealing screws to reduce leakage under fast MAS. The utility of these rotors is maximized when they are used in conjunction with a novel methodology known as combined liquid- and solid-state in situ crystallization (CLASSIC) NMR, by which Harris and colleagues (147) studied in situ crystallization. The CLASSIC methodology initially features real-time sequential NMR acquisition by using  $^1\text{H}$ – $^{13}\text{C}$  CP and  $^{13}\text{C}$  direct excitation for probing reactions at solid–liquid interfaces and in the liquid phase, respectively. This method, utilizing  $^{27}\text{Al}$  MQMAS and  $^{27}\text{Al}$  direct excitation, has been recently applied to the investigation of the hydration of calcium aluminate cement by tracking the variations in the fraction of different Al sites (4- or 6-coordination) as a function of time (148). Another new MAS rotor design—dubbed WHiMS after the names of the inventors, Walter, Hoyt, Mehta, and Sears (149)—enables in situ NMR studies of heterogeneous catalysis at pressures in excess of 200 bar at 250°C. Using WHiMS, the time/temperature/pressure dependence of reaction kinetics of benzyl phenyl ether hydrogenolysis catalyzed by  $\text{Ni}/\gamma\text{-Al}_2\text{O}_3$  in the presence of  $\text{H}_{2(\text{g})}$  or isopropanol<sub>(l)</sub> is demonstrated with operando high-resolution  $^1\text{H}$  and  $^{13}\text{C}$  MAS spectra to track the growth of products such as toluene and phenol (149). Hoyt and colleagues (149) further improved the design to allow NMR acquisitions at temperatures and pressures up to 325°C and 400 bar, respectively. Notably, supercritical fluids such as supercritical  $\text{CO}_2$  can be safely contained in WHiMS rotors during high-temperature and -pressure NMR experiments, which enables a number of geoscience applications (150).

Pressure-induced changes in physical phenomena such as structural, metal–insulator, and superconducting phase transitions have attracted great attention since these behaviors are related to fundamental questions both in materials and life sciences (151, 152). High-pressure NMR generally exploits diamond anvil cells (DACs) (153), in which a very small amount of analyte ( $<10^{-9}$  L) is placed in a gasket centered between two diamond anvils. NMR employing DACs suffers from low sensitivity; therefore, it requires a reasonable filling factor of the RF coil (a high filling factor indicates that the analyte closely fits the space in the coil). This imposes a technical challenge: The RF coil needs to be placed as close as possible to the sample while avoiding severe deformation

under pressure. This obstacle is alleviated to some extent by using microcoils (151), but microcoils are fragile and not widely adopted. In 2017, Meier et al. (153) introduced a Lenz resonator that produces a  $B_1$  field inductively coupled to the excitation coil to focus the magnetic flux at the central region where the analyte resides, thereby locally enhancing detection sensitivity. The stable  $B_1$  field permits a Larmor frequency-dependent limit of detection of  $1.5 \times 10^{12}$  spins  $\text{Hz}^{-0.5}$  up to 72 GPa. More recently, the same group made high-pressure NMR measurements up to 90 GPa (154). Sen and colleagues (155) demonstrated the application of an in situ high-pressure cell (up to 2 GPa) equipped with pressure-transmitting fluid (paraffin oil) to study pressure-induced  $\text{BO}_3 \rightarrow \text{BO}_4$  phase conversions in borosilicate glasses. In addition to probing distinct phase transitions, high-pressure NMR also enables the investigation of more subtle changes in coordination environments, for instance, the interplay between pressure and the collapse of the tetrahedral framework that accommodates  $\text{Na}^+$  cations in albite (156). Understanding structural changes is critical to the improvement of physical properties of glassy materials, and high-pressure NMR encourages in-depth exploration of structure–property relations associated with pressure.

Low sensitivity restricts in situ NMR studies especially when high temporal resolution is required to track fast changes. Typically, the in situ NMR setup for investigating electrochemical processes such as in rechargeable batteries, fuel cells, and supercapacitors results in more sensitivity reduction due to the mismatch between solenoid coils and pouch cells yielding low filling factors. In this context, Sorte, Tong, and colleagues (157) developed a novel stripline detector that is sandwiched between an anode and a cathode where it acts as a current collector and, more importantly, as an RF-confining/homogenizing plate. With this detector, the generated  $B_1$  field is confined within a long but narrow region (aspect ratio of  $\sim 5$ ), which is fully covered by the analyte (typically a composite electrode in these electrochemical energy applications), enabling a high filling factor and, thus, enhanced sensitivity. The robustness of this design was tested by running in situ stripline NMR on  $\text{LiFePO}_4$ ,  $\text{LiCoO}_2$ , and LG commercial cells as a function of the state of charge. With enhanced sensitivity, the in situ stripline NMR detector allows the observation of intermediate phases generated during electrochemical cycling.

The RF excitation pulses used to acquire solid-state NMR spectra are manually tuned and matched to the resonant frequency of the nucleus of interest with variable capacitors. These pulses typically have a bandwidth on the order of 100 kHz, which is wide enough to fully excite most diamagnetic and nonquadrupolar systems. When extremely broadband excitation and/or multinuclear NMR is necessary for in situ acquisitions, or when structurally induced NMR shift variations occur upon exposure of the samples to external stimuli, retuning/matching the transmitter resonance circuit is required. Grey and colleagues (158, 159) recently incorporated an automatic tuning matching cyler robot with standard NMR probes, enabling on-the-fly recalibration of the transmitter frequency. This innovation is particularly beneficial to NMR users who need to repeat experiments as a function of time, temperature, pressure, or any factors that will change the property of the analytes during measurements and lead to changes in the RF circuit (160).

In summary, continuous innovation of NMR hardware has been made to address various challenges that arise for in situ NMR acquisition and NMR under extreme conditions. These new hardware developments allow the observation of transient phenomena with high temporal resolution and structural insights of material properties that only exist under extreme temperature/pressure/electric field/magnetic field conditions.

## 8. CONCLUDING REMARKS

Recent advancements in solid-state NMR and MRI have yielded enhanced sensitivity and spectral/spatial/temporal resolution with increased capabilities for probing atomic correlations and

dynamics, which makes them increasingly more powerful techniques for materials research. The high demand for materials characterizations in situ/operando and/or under extreme conditions inspires further innovation in solid-state NMR/MRI techniques and hardware.

## DISCLOSURE STATEMENT

The authors are not aware of any affiliations, memberships, funding, or financial holdings that might be perceived as affecting the objectivity of this review.

## ACKNOWLEDGMENTS

P.-H.C. and Y.-Y.H. were supported by the National Science Foundation (DMR-1808517). K.J.G. acknowledges support from the Joint Center for Energy Storage Research, an energy innovation hub funded by the US Department of Energy, Office of Science, Basic Energy Sciences. H.L. acknowledges support from the National Science Foundation under the grant 1847038. Z.G. acknowledges support from the National High Magnetic Field Laboratory, which is funded by the National Science Foundation through NSF/DMR-1644779 and the state of Florida.

## LITERATURE CITED

1. Hung I, Gan Z. 2018. Isotropic versus anisotropic chemical shift separation. In *Modern Methods in Solid-State NMR: A Practitioner's Guide*, ed. P Hodgkinson, pp. 75–96. Cambridge, UK: R. Soc. Chem.
2. Liao W-C, Ghaffari B, Gordon CP, Xu J, Copéret C. 2018. Dynamic nuclear polarization surface enhanced NMR spectroscopy (DNP SENS): principles, protocols, and practice. *Curr. Opin. Colloid Interface Sci.* 33:63–71
3. Yi X, Liu K, Chen W, Li J, Xu S, et al. 2018. Origin and structural characteristics of tri-coordinated extra-framework aluminum species in dealuminated zeolites. *J. Am. Chem. Soc.* 140(34):10764–74
4. Kärger J, Freude D, Haase J. 2018. Diffusion in nanoporous materials: novel insights by combining MAS and PFG NMR. *Processes* 6(9):147
5. Bottke P, Rettenwander D, Schmidt W, Amthauer G, Wilkening M. 2015. Ion dynamics in solid electrolytes: NMR reveals the elementary steps of Li<sup>+</sup> hopping in the garnet Li<sub>6.5</sub>La<sub>3</sub>Zr<sub>1.75</sub>Mo<sub>0.25</sub>O<sub>12</sub>. *Chem. Mater.* 27(19):6571–82
6. Romanenko K, Jin L, Howlett P, Forsyth M. 2016. In situ MRI of operating solid-state lithium metal cells based on ionic plastic crystal electrolytes. *Chem. Mater.* 28(8):2844–51
7. Chien P-H, Feng X, Tang M, Rosenberg JT, O'Neill S, et al. 2018. Li distribution heterogeneity in solid electrolyte Li<sub>10</sub>GeP<sub>2</sub>S<sub>12</sub> upon electrochemical cycling probed by <sup>7</sup>Li MRI. *J. Phys. Chem. Lett.* 9(8):1990–98
8. Paruzzo FM, Hofstetter A, Musil F, De S, Ceriotti M, Emsley L. 2018. Chemical shifts in molecular solids by machine learning. *Nat. Commun.* 9(1):4501
9. Keeler J. 2010. *Understanding NMR Spectroscopy*. West Sussex, UK: John Wiley & Sons. 2nd ed.
10. Slichter CP. 2010. *Principles of Magnetic Resonance*. Berlin/Heidelberg, Ger.: Springer
11. Schmidt-Rohr K, Spiess HW, eds. 1994. *Multidimensional Solid-State NMR and Polymers*. San Diego: Academic
12. Apperley DC, Harris RK, Hodgkinson P. 2012. *Solid-State NMR: Basic Principles and Practice*. New York: Monumentum
13. Callaghan PT. 1994. *Principles of Nuclear Magnetic Resonance Microscopy*. Oxford, UK: Clarendon
14. Melinda J. Duer. 2005. *Introduction to Solid-State NMR Spectroscopy*. Oxford, UK: Blackwell
15. Levitt MH. 2008. *Spin Dynamics: Basics of Nuclear Magnetic Resonance*. Chichester, UK: John Wiley & Sons
16. Ernst RR, Bodenhausen G, Wokaun A. 1987. *Principles of Nuclear Magnetic Resonance in One and Two Dimensions*. Oxford, UK: Clarendon

17. Andrew ER, Bradbury A, Eades RG. 1959. Removal of dipolar broadening of nuclear magnetic resonance spectra of solids by specimen rotation. *Nature* 183(4678):1802–3
18. Lowe IJ. 1959. Free induction decays of rotating solids. *Phys. Rev. Lett.* 2(7):285–87
19. Polenova T, Gupta R, Goldbourt A. 2015. Magic angle spinning NMR spectroscopy: a versatile technique for structural and dynamic analysis of solid-phase systems. *Anal. Chem.* 87(11):5458–69
20. Agarwal V, Penzel S, Szekely K, Cadalbert R, Testori E, et al. 2014. De novo 3D structure determination from sub-milligram protein samples by solid-state 100 kHz MAS NMR spectroscopy. *Angew. Chem. Int. Ed.* 53(45):12253–56
21. Mroue KH, Nishiyama Y, Kumar Pandey M, Gong B, McNerny E, et al. 2015. Proton-detected solid-state NMR spectroscopy of bone with ultrafast magic angle spinning. *Sci. Rep.* 5(1):11991
22. Xue K, Sarkar R, Motz C, Asami S, Camargo DCR, et al. 2017. Limits of resolution and sensitivity of proton detected MAS solid-state NMR experiments at 111 kHz in deuterated and protonated proteins. *Sci. Rep.* 7(1):7444
23. David G, Fogeron M-L, Schledorn M, Montserret R, Haselmann U, et al. 2018. Structural studies of self-assembled subviral particles: combining cell-free expression with 110 kHz MAS NMR spectroscopy. *Angew. Chem. Int. Ed.* 57(17):4787–91
24. Zhang R, Mroue KH, Ramamoorthy A. 2017. Proton-based ultrafast magic angle spinning solid-state NMR spectroscopy. *Acc. Chem. Res.* 50(4):1105–13
25. Penzel S, Oss A, Org M-L, Samoson A, Böckmann A, et al. 2019. Spinning faster: protein NMR at MAS frequencies up to 126 kHz. *J. Biomol. NMR* 73(1–2):19–29
26. Chen P, Albert BJ, Gao C, Alaniva N, Price LE, et al. 2018. Magic angle spinning spheres. *Sci. Adv.* 4(9):eaau1540
27. Kentgens APM. 1997. A practical guide to solid-state NMR of half-integer quadrupolar nuclei with some applications to disordered systems. *Geoderma* 80(3–4):271–306
28. Frydman L. 2002. Fundamentals of multiple-quantum magic-angle spinning NMR on half-integer quadrupolar nuclei. In *Encyclopedia of Nuclear Magnetic Resonance*, Vol. 9: *Advances in NMR*, ed. DM Grant, RK Harris, pp. 262–74. Chichester, UK: John Wiley & Sons
29. Ashbrook SE, Sneddon S. 2014. New methods and applications in solid-state NMR spectroscopy of quadrupolar nuclei. *J. Am. Chem. Soc.* 136(44):15440–56
30. Wasylishen RE, Ashbrook SE, Wimperis S, eds. 2012. *NMR of Quadrupolar Nuclei in Solid Materials*. Chichester, UK: Wiley
31. Cozzan C, Griffith KJ, Laurita G, Hu JG, Grey CP, Seshadri R. 2017. Structural evolution and atom clustering in  $\beta$ -SiAlON:  $\beta$ -Si<sub>6-z</sub>Al<sub>z</sub>O<sub>z</sub>N<sub>8-z</sub>. *Inorg. Chem.* 56(4):2153–58
32. Frydman L, Harwood JS. 1995. Isotropic spectra of half-integer quadrupolar spins from bidimensional magic-angle spinning NMR. *J. Am. Chem. Soc.* 117(19):5367–68
33. Medek A, Harwood JS, Frydman L. 1995. Multiple-quantum magic-angle spinning NMR: a new method for the study of quadrupolar nuclei in solids. *J. Am. Chem. Soc.* 117(51):12779–87
34. Massiot D, Fayon F, Capron M, King I, Le Calvé S, et al. 2002. Modelling one- and two-dimensional solid-state NMR spectra: modelling 1D and 2D solid-state NMR spectra. *Magn. Reson. Chem.* 40(1):70–76
35. Gan Z. 2001. Satellite transition magic-angle spinning nuclear magnetic resonance spectroscopy of half-integer quadrupolar nuclei. *J. Chem. Phys.* 114(24):10845–53
36. Gan Z. 2000. Isotropic NMR spectra of half-integer quadrupolar nuclei using satellite transitions and magic-angle spinning. *J. Am. Chem. Soc.* 122(13):3242–43
37. Samoson A, Lippmaa E, Pines A. 1988. High resolution solid-state N.M.R. *Mol. Phys.* 65(4):1013–18
38. Llor A, Virlet J. 1988. Towards high-resolution NMR of more nuclei in solids: sample spinning with time-dependent spinner axis angle. *Chem. Phys. Lett.* 152(2–3):248–53
39. Pell AJ, Pintacuda G, Grey CP. 2019. Paramagnetic NMR in solution and the solid state. *Prog. Nucl. Magn. Reson. Spectrosc.* 111:1–271
40. Hung I, Zhou L, Pourpoint F, Grey CP, Gan Z. 2012. Isotropic high field NMR spectra of Li-ion battery materials with anisotropy > 1 MHz. *J. Am. Chem. Soc.* 134(4):1898–901
41. Hu JZ, Alderman DW, Ye C, Pugmire RJ, Grant DM. 1993. An isotropic chemical shift-chemical shift anisotropy magic-angle slow-spinning 2D NMR experiment. *J. Magn. Reson. Ser. A* 105(1):82–87

42. Dixon WT. 1982. Spinning-sideband-free and spinning-sideband-only NMR spectra in spinning samples. *J. Chem. Phys.* 77(4):1800–9
43. Gan Z. 1992. High-resolution chemical shift and chemical shift anisotropy correlation in solids using slow magic angle spinning. *J. Am. Chem. Soc.* 114(21):8307–9
44. Whittles Z, Marple M, Hung I, Gan Z, Sen S. 2018. Structure of BaO–TeO<sub>2</sub> glasses: a two-dimensional <sup>125</sup>Te NMR spectroscopic study. *J. Non-Crystalline Solids* 481:282–88
45. Stobridge FC, Middlemiss DS, Pell AJ, Leskes M, Clément RJ, et al. 2014. Characterising local environments in high energy density Li-ion battery cathodes: a combined NMR and first principles study of LiFe<sub>x</sub>Co<sub>1-x</sub>PO<sub>4</sub>. *J. Mater. Chem. A.* 2(30):11948–57
46. Li X, Tang M, Feng X, Hung I, Rose A, et al. 2017. Lithiation and delithiation dynamics of different Li sites in Li-rich battery cathodes studied by *operando* nuclear magnetic resonance. *Chem. Mater.* 29(19):8282–91
47. Feng X-Y, Chien P-H, Rose AM, Zheng J, Hung I, et al. 2016. Cr<sub>2</sub>O<sub>5</sub> as new cathode for rechargeable sodium ion batteries. *J. Solid State Chem.* 242:96–101
48. Schurko RW. 2013. Ultra-wideline solid-state NMR spectroscopy. *Acc. Chem. Res.* 46(9):1985–95
49. Smith PES, Donovan KJ, Szekely O, Baias M, Frydman L. 2013. Ultrafast NMR *T*<sub>1</sub> relaxation measurements: probing molecular properties in real time. *Chem. Phys. Chem.* 14(13):3138–45
50. Clément RJ, Pell AJ, Middlemiss DS, Stobridge FC, Miller JK, et al. 2012. Spin-transfer pathways in paramagnetic lithium transition-metal phosphates from combined broadband isotropic solid-state MAS NMR spectroscopy and DFT calculations. *J. Am. Chem. Soc.* 134(41):17178–85
51. Sesti EL, Alaniva N, Rand PW, Choi EJ, Albert BJ, et al. 2018. Magic angle spinning NMR below 6 K with a computational fluid dynamics analysis of fluid flow and temperature gradients. *J. Magn. Reson.* 286:1–9
52. Frydman L. 2014. High magnetic field science and its application in the United States: a magnetic resonance perspective. *J. Magn. Reson.* 242:256–64
53. Hartmann SR, Hahn EL. 1962. Nuclear double resonance in the rotating frame. *Phys. Rev.* 128(5):2042–53
54. Pines A, Gibby MG, Waugh JS. 1972. Proton-enhanced nuclear induction spectroscopy. A method for high resolution NMR of dilute spins in solids. *J. Chem. Phys.* 56(4):1776–77
55. Paluch P, Potrzebowska N, Ruppert AM, Potrzebowski MJ. 2017. Application of <sup>1</sup>H and <sup>27</sup>Al magic angle spinning solid state NMR at 60 kHz for studies of Au and Au–Ni catalysts supported on boehmite/alumina. *Solid State Nucl. Magn. Reson.* 84:111–17
56. Xue X, Kanzaki M, Turner D, Loroch D. 2017. Hydrogen incorporation mechanisms in forsterite: new insights from <sup>1</sup>H and <sup>29</sup>Si NMR spectroscopy and first-principles calculation. *Am. Mineral.* 102(3):519–36
57. Kolodziejcki W, Klinowski J. 2002. Kinetics of cross-polarization in solid-state NMR: a guide for chemists. *Chem. Rev.* 102(3):613–28
58. Johnson RL, Schmidt-Rohr K. 2014. Quantitative solid-state <sup>13</sup>C NMR with signal enhancement by multiple cross polarization. *J. Magn. Reson.* 239:44–49
59. Vega AJ. 1992. CP/MAS of quadrupolar *S* = 3/2 nuclei. *Solid State Nucl. Magn. Reson.* 1:17–32
60. Perras FA, Kobayashi T, Pruski M. 2015. PRESTO polarization transfer to quadrupolar nuclei: implications for dynamic nuclear polarization. *Phys. Chem. Chem. Phys.* 17(35):22616–22
61. Althaus SM, Mao K, Stringer JA, Kobayashi T, Pruski M. 2014. Indirectly detected heteronuclear correlation solid-state NMR spectroscopy of naturally abundant <sup>15</sup>N nuclei. *Solid State Nucl. Magn. Reson.* 57–58:17–21
62. Wiench JW, Bronnimann CE, Lin VS-Y, Pruski M. 2007. Chemical shift correlation NMR spectroscopy with indirect detection in fast rotating solids: studies of organically functionalized mesoporous silicas. *J. Am. Chem. Soc.* 129:12076–77
63. Hu B, Trébose J, Amoureux JP. 2008. Comparison of several hetero-nuclear dipolar recoupling NMR methods to be used in MAS HMQC/HSQC. *J. Magn. Reson.* 192(1):112–22
64. Gan Z. 2006. Measuring amide nitrogen quadrupolar coupling by high-resolution <sup>14</sup>N/<sup>13</sup>C NMR correlation under magic-angle spinning. *J. Am. Chem. Soc.* 128(18):6040–41

65. Venkatesh A, Hanrahan MP, Rossini AJ. 2017. Proton detection of MAS solid-state NMR spectra of half-integer quadrupolar nuclei. *Solid State Nucl. Magn. Reson.* 84:171–81
66. Schanda P, Kupče Ě, Brutscher B. 2005. SOFAST-HMQC experiments for recording two-dimensional heteronuclear correlation spectra of proteins within a few seconds. *J. Biomol. NMR* 33(4):199–211
67. Hung I, Gan Z. 2010. On the practical aspects of recording wide-line QCPMG NMR spectra. *J. Magn. Reson.* 204(2):256–65
68. Jardón-Álvarez D, Bovee MO, Baltisberger JH, Grandinetti PJ. 2019. Natural abundance  $^{17}\text{O}$  and  $^{33}\text{S}$  nuclear magnetic resonance spectroscopy in solids achieved through extended coherence lifetimes. *Phys. Rev. B* 100(14):140103
69. Vosegaard T, Larsen FH, Jakobsen HJ, Ellis PD, Nielsen NC. 1997. Sensitivity-enhanced multiple-quantum MAS NMR of half-integer quadrupolar nuclei. *J. Am. Chem. Soc.* 119(38):9055–56
70. Hung I, Gan Z. 2014. Fast REDOR with CPMG multiple-echo acquisition. *J. Magn. Reson.* 238:82–86
71. Hung I, Edwards T, Sen S, Gan Z. 2012. MATPASS/CPMG: a sensitivity enhanced magic-angle spinning sideband separation experiment for disordered solids. *J. Magn. Reson.* 221:103–9
72. Harris KJ, Lupulescu A, Lucier BEG, Frydman L, Schurko RW. 2012. Broadband adiabatic inversion pulses for cross polarization in wide-line solid-state NMR spectroscopy. *J. Magn. Reson.* 224:38–47
73. O'Dell LA. 2013. The WURST kind of pulses in solid-state NMR. *Solid State Nucl. Magn. Reson.* 55–56:28–41
74. Green RA, Adams RW, Duckett SB, Mewis RE, Williamson DC, Green GGR. 2012. The theory and practice of hyperpolarization in magnetic resonance using parahydrogen. *Prog. Nucl. Magn. Reson. Spectrosc.* 67:1–48
75. Lilly Thankamony AS, Wittmann JJ, Kaushik M, Corzilius B. 2017. Dynamic nuclear polarization for sensitivity enhancement in modern solid-state NMR. *Prog. Nucl. Magn. Reson. Spectrosc.* 102–103:120–95
76. Willmerring MM, Ma ZL, Jenkins MA, Conley JF, Hayes SE. 2017. Enhanced NMR with optical pumping yields  $^{75}\text{As}$  signals selectively from a buried GaAs interface. *J. Am. Chem. Soc.* 139(11):3930–33
77. Zhao EW, Maligal-Ganesh R, Du Y, Zhao TY, Collins J, et al. 2018. Surface-mediated hyperpolarization of liquid water from parahydrogen. *Chemistry* 4(6):1387–403
78. Overhauser AW. 1953. Polarization of nuclei in metals. *Phys. Rev.* 92(2):411–15
79. Carver TR, Slichter CP. 1953. Polarization of nuclear spins in metals. *Phys. Rev.* 92(1):212–13
80. Rossini AJ, Zagdoun A, Lelli M, Lesage A, Copéret C, Emsley L. 2013. Dynamic nuclear polarization surface enhanced NMR spectroscopy. *Acc. Chem. Res.* 46(9):1942–51
81. Ni QZ, Daviso E, Can TV, Markhasin E, Jawla SK, et al. 2013. High frequency dynamic nuclear polarization. *Acc. Chem. Res.* 46(9):1933–41
82. Sauvé C, Rosay M, Casano G, Aussenac F, Weber RT, et al. 2013. Highly efficient, water-soluble polarizing agents for dynamic nuclear polarization at high frequency. *Angew. Chem. Int. Ed.* 52(41):10858–61
83. Zagdoun A, Casano G, Ouari O, Schwarzwälder M, Rossini AJ, et al. 2013. Large molecular weight nitroxide biradicals providing efficient dynamic nuclear polarization at temperatures up to 200 K. *J. Am. Chem. Soc.* 135(34):12790–97
84. Piveteau L, Ong T-C, Walder BJ, Dirin DN, Moscheni D, et al. 2018. Resolving the core and the surface of CdSe quantum dots and nanoplatelets using dynamic nuclear polarization enhanced PASS-PIETA NMR spectroscopy. *ACS Cent. Sci.* 4(9):1113–25
85. Lelli M, Gajan D, Lesage A, Caporini MA, Vitzthum V, et al. 2011. Fast characterization of functionalized silica materials by silicon-29 surface-enhanced NMR spectroscopy using dynamic nuclear polarization. *J. Am. Chem. Soc.* 133(7):2104–7
86. Chakrabarty T, Goldin N, Feintuch A, Houben L, Leskes M. 2018. Paramagnetic metal-ion dopants as polarization agents for dynamic nuclear polarization NMR spectroscopy in inorganic solids. *Chem. Phys. Chem.* 19(17):2139–42
87. Hope MA, Rinkel BL, Gunnarsdóttir AB, Märker K, Menkin S, et al. 2020. Selective NMR observation of the SEI-metal interface by dynamic nuclear polarisation from lithium metal. *Nature Comm.* 11(1):2224
88. Eckert H. 2018. Spying with spins on messy materials: 60 years of glass structure elucidation by NMR spectroscopy. *Int. J. Appl. Glass Sci.* 9(2):167–87



89. Eckert H. 1992. Structural characterization of noncrystalline solids and glasses using solid state NMR. *Prog. Nucl. Magn. Reson. Spectrosc.* 24(3):159–293
90. Bertmer M, Eckert H. 1999. Dephasing of spin echoes by multiple heteronuclear dipolar interactions in rotational echo double resonance NMR experiments. *Solid State Nucl. Magn. Reson.* 15(3):139–52
91. Ren J, Eckert H. 2018. Superstructural units involving six-coordinated silicon in sodium phosphosilicate glasses detected by solid-state NMR spectroscopy. *J. Phys. Chem. C* 122(48):27620–30
92. Santagneli SH, Baldacim HVA, Ribeiro SJL, Kundu S, Rodrigues ACM, et al. 2016. Preparation, structural characterization, and electrical conductivity of highly ion-conducting glasses and glass ceramics in the system  $\text{Li}_{1+x}\text{Al}_x\text{Sn}_y\text{Ge}_{2-(x+y)}(\text{PO}_4)_3$ . *J. Phys. Chem. C* 120(27):14556–67
93. Hu Y-Y, Rawal A, Schmidt-Rohr K. 2010. Strongly bound citrate stabilizes the apatite nanocrystals in bone. *PNAS* 107(52):22425–29
94. Kong X, Deng H, Yan F, Kim J, Swisher JA, et al. 2013. Mapping of functional groups in metal-organic frameworks. *Science* 341(6148):882–85
95. Hing AW, Vega S, Schaefer J. 1992. Transferred-echo double-resonance NMR. *J. Magn. Reson.* 1969 96(1):205–9
96. Bodart PR, Delmotte L, Rigolet S, Brendlé J, Gougeon RD. 2018.  $^7\text{Li}\{^{19}\text{F}\}$  TEDOR NMR to observe the lithium migration in heated montmorillonite. *Appl. Clay Sci.* 157:204–11
97. Grey CP, Vega AJ. 1995. Determination of the quadrupole coupling constant of the invisible aluminum spins in zeolite HY with  $^1\text{H}/^{27}\text{Al}$  TRAPDOR NMR. *J. Am. Chem. Soc.* 117(31):8232–42
98. Gullion T. 1995. Measurement of dipolar interactions between spin-1/2 and quadrupolar nuclei by rotational-echo, adiabatic-passages, double-resonance NMR. *Chem. Phys. Lett.* 246(3):325–30
99. Gan Z. 2006. Measuring multiple carbon–nitrogen distances in natural abundant solids using R-RESPDOR NMR. *Chem. Commun.* 45:4712–14
100. Chen L, Wang Q, Hu B, Lafon O, Trébois J, et al. 2010. Measurement of hetero-nuclear distances using a symmetry-based pulse sequence in solid-state NMR. *Phys. Chem. Chem. Phys.* 12:9395–405
101. Rankin AGM, Webb PB, Dawson DM, Viger-Gravel J, Walder BJ, et al. 2017. Determining the surface structure of silicated alumina catalysts via isotopic enrichment and dynamic nuclear polarization surface-enhanced NMR spectroscopy. *J. Phys. Chem. C* 121(41):22977–84
102. Fitzgerald JJ, DePaul SM. 1999. Solid-state NMR spectroscopy of inorganic materials: an overview. In *Solid-State NMR Spectroscopy of Inorganic Materials*, ed. JJ Fitzgerald, pp. 2–133. Washington, DC: Am. Chem. Soc.
103. Zheng A, Liu S-B, Deng F. 2017.  $^{31}\text{P}$  NMR chemical shifts of phosphorus probes as reliable and practical acidity scales for solid and liquid catalysts. *Chem. Rev.* 117(19):12475–531
104. Zoubida L, Hichem B. 2018. The nanostructure zeolites MFI-type ZSM5. In *Nanocrystals and Nanostructures*, ed. CM Simionescu, pp. 43–62. London: InTechOpen
105. Valla M, Rossini AJ, Caillot M, Chizallet C, Raybaud P, et al. 2015. Atomic description of the interface between silica and alumina in aluminosilicates through dynamic nuclear polarization surface-enhanced NMR spectroscopy and first-principles calculations. *J. Am. Chem. Soc.* 137(33):10710–19
106. Bennett AE, Griffin RG, Ok JH, Vega S. 1992. Chemical shift correlation spectroscopy in rotating solids: radio frequency-driven dipolar recoupling and longitudinal exchange. *J. Chem. Phys.* 96(11):8624–27
107. Mao J, Cao X, Olk DC, Chu W, Schmidt-Rohr K. 2017. Advanced solid-state NMR spectroscopy of natural organic matter. *Prog. Nucl. Magn. Reson. Spectrosc.* 100:17–51
108. deAzevedo ER, Bonagamba TJ, Schmidt-Rohr K. 2000. Pure-exchange solid-state NMR. *J. Magn. Reson.* 142(1):86–96
109. Krajnc A, Kos T, Zabukovec Logar N, Mali G. 2015. A simple NMR-based method for studying the spatial distribution of linkers within mixed-linker metal-organic frameworks. *Angew. Chem. Int. Ed.* 54(36):10535–38
110. Krajnc A, Bueken B, De Vos D, Mali G. 2017. Improved resolution and simplification of the spin-diffusion-based NMR method for the structural analysis of mixed-linker MOFs. *J. Magn. Reson.* 279:22–28
111. Ba Y, Veeman WS. 1993. Experimental detection of multiple-quantum coherence transfer in coupled spin solids by multi-dimensional NMR experiments. *Solid State Nucl. Magn. Reson.* 2(3):131–41

112. Brouwer DH, Kristiansen PE, Fyfe CA, Levitt MH. 2005. Symmetry-based  $^{29}\text{Si}$  dipolar recoupling magic angle spinning NMR spectroscopy: a new method for investigating three-dimensional structures of zeolite frameworks. *J. Am. Chem. Soc.* 127(2):542–43
113. Kobayashi T, Singappuli-Arachchige D, Wang Z, Slowing II, Pruski M. 2017. Spatial distribution of organic functional groups supported on mesoporous silica nanoparticles: a study by conventional and DNP-enhanced  $^{29}\text{Si}$  solid-state NMR. *Phys. Chem. Chem. Phys.* 19(3):1781–89
114. Hohwy M, Rienstra CM, Jaroniec CP, Griffin RG. 1999. Fivefold symmetric homonuclear dipolar recoupling in rotating solids: application to double quantum spectroscopy. *J. Chem. Phys.* 110(16):7983–92
115. Smeets S, Berkson ZJ, Xie D, Zones SI, Wan W, et al. 2017. Well-defined silanols in the structure of the calcined high-silica zeolite SSZ-70: new understanding of a successful catalytic material. *J. Am. Chem. Soc.* 139(46):16803–12
116. Teymoori G, Pahari B, Viswanathan E, Edén M. 2013. Multiple-quantum spin counting in magic-angle-spinning NMR via low-power symmetry-based dipolar recoupling. *J. Magn. Reson.* 236:31–40
117. Hong M, DeGrado WF. 2012. Structural basis for proton conduction and inhibition by the influenza M2 protein. *Protein Sci.* 21(11):1620–33
118. Haile SM, Boysen DA, Chisholm CRI, Merle RB. 2001. Solid acids as fuel cell electrolytes. *Nature* 410(6831):910–13
119. Chien P-H, Jee Y, Huang C, Dervişoğlu R, Hung I, et al. 2016. On the origin of high ionic conductivity in Na-doped  $\text{SrSiO}_3$ . *Chem. Sci.* 7(6):3667–75
120. Liang X, Wang L, Jiang Y, Wang J, Luo H, et al. 2015. In-channel and in-plane Li ion diffusions in the superionic conductor  $\text{Li}_{10}\text{GeP}_2\text{S}_{12}$  probed by solid-state NMR. *Chem. Mater.* 27(16):5503–10
121. Vyalikh A, Schikora M, Seipel KP, Weigler M, Zschornak M, et al. 2019. NMR studies of Li mobility in NASICON-type glass-ceramic ionic conductors with optimized microstructure. *J. Mater. Chem. A* 7(23):13968–77
122. Forse AC, Griffin JM, Merlet C, Bayley PM, Wang H, et al. 2015. NMR study of ion dynamics and charge storage in ionic liquid supercapacitors. *J. Am. Chem. Soc.* 137(22):7231–42
123. Pampel A, Zick K, Glauner H, Engelke F. 2004. Studying lateral diffusion in lipid bilayers by combining a magic angle spinning NMR probe with a microimaging gradient system. *J. Am. Chem. Soc.* 126(31):9534–35
124. Callaghan PT, Coy A, MacGowan D, Packer KJ, Zelaya FO. 1991. Diffraction-like effects in NMR diffusion studies of fluids in porous solids. *Nature* 351(6326):467–69
125. Hayamizu K, Terada Y, Kataoka K, Akimoto J. 2019. Toward understanding the anomalous Li diffusion in inorganic solid electrolytes by studying a single-crystal garnet of LLZO-Ta by pulsed-gradient spin-echo nuclear magnetic resonance spectroscopy. *J. Chem. Phys.* 150(19):194502
126. Wilkening M, Heitjans P. 2012. From micro to macro: access to long-range  $\text{Li}^+$  diffusion parameters in solids via microscopic  $^6,7\text{Li}$  spin-alignment echo NMR spectroscopy. *Chem. Phys. Chem.* 13(1):53–65
127. Heitjans P, Schirmer A, Indris S. 2005. NMR and  $\beta$ -NMR studies of diffusion in interface-dominated and disordered solids. In *Diffusion in Condensed Matter: Methods, Materials, Models*, ed. P Heitjans, J Kärger, pp. 367–416. Berlin/Heidelberg, Ger.: Springer-Verlag. 2nd ed.
128. Epp V, Gün Ö, Deiseroth H-J, Wilkening M. 2013. Highly mobile ions: low-temperature NMR directly probes extremely fast  $\text{Li}^+$  hopping in argyrodite-type  $\text{Li}_6\text{PS}_5\text{Br}$ . *J. Phys. Chem. Lett.* 4(13):2118–23
129. Breuer S, Gombotz M, Pregartner V, Hanzu I, Wilkening M. 2019. Heterogeneous F anion transport, local dynamics and electrochemical stability of nanocrystalline  $\text{La}_{1-x}\text{Ba}_x\text{F}_{3-x}$ . *Energy Storage Mater.* 16:481–90
130. Hanghofer I, Redhammer GJ, Rohde S, Hanzu I, Senyshyn A, et al. 2018. Untangling the structure and dynamics of lithium-rich anti-perovskites envisaged as solid electrolytes for batteries. *Chem. Mater.* 30(22):8134–44
131. Storek M, Böhmer R. 2016. Interchannel hopping in single crystalline lithium triborate probed by  $^7\text{Li}$  NMR: spin relaxation, line shape analysis, selective-inversion spin alignment, and two-dimensional exchange spectra. *J. Phys. Chem. C* 120(14):7767–77
132. Bottke P, Freude D, Wilkening M. 2013. Ultraslow Li exchange processes in diamagnetic  $\text{Li}_2\text{ZrO}_3$  As monitored by EXSY NMR. *J. Phys. Chem. C* 117(16):8114–19

133. Wang D, Zhong G, Pang WK, Guo Z, Li Y, et al. 2015. Toward understanding the lithium transport mechanism in garnet-type solid electrolytes:  $\text{Li}^+$  ion exchanges and their mobility at octahedral/tetrahedral sites. *Chem. Mater.* 27(19):6650–59
134. Yu C, Ganapathy S, van Eck ERH, Wang H, Basak S, et al. 2017. Accessing the bottleneck in all-solid state batteries, lithium-ion transport over the solid-electrolyte-electrode interface. *Nat. Commun.* 8(1):1086
135. Westbrook C, Talbot J. 2019. *MRI in Practice*. Hoboken, NJ: John Wiley & Sons. 5th ed.
136. Romanenko K, Forsyth M, O'Dell LA. 2014. New opportunities for quantitative and time efficient 3D MRI of liquid and solid electrochemical cell components: sectoral fast spin echo and SPRITE. *J. Magn. Reson.* 248:96–104
137. Bray JM, Davenport AJ, Ryder KS, Britton MM. 2016. Quantitative, in situ visualization of metal-ion dissolution and transport using  $^1\text{H}$  magnetic resonance imaging. *Angew. Chem. Int. Ed.* 55(32):9394–97
138. Ilott AJ, Mohammadi M, Schauerman CM, Ganter MJ, Jerschow A. 2018. Rechargeable lithium-ion cell state of charge and defect detection by in-situ inside-out magnetic resonance imaging. *Nat. Commun.* 9(1):1776
139. Krachkovskiy SA, Bazak JD, Werhun P, Balcom BJ, Halalay IC, Goward GR. 2016. Visualization of steady-state ionic concentration profiles formed in electrolytes during Li-ion battery operation and determination of mass-transport properties by in situ magnetic resonance imaging. *J. Am. Chem. Soc.* 138(25):7992–99
140. Chang HJ, Ilott AJ, Trease NM, Mohammadi M, Jerschow A, Grey CP. 2015. Correlating microstructural lithium metal growth with electrolyte salt depletion in lithium batteries using  $^7\text{Li}$  MRI. *J. Am. Chem. Soc.* 137(48):15209–16
141. Chandrashekar S, Trease NM, Chang HJ, Du L-S, Grey CP, Jerschow A. 2012.  $^7\text{Li}$  MRI of Li batteries reveals location of microstructural lithium. *Nat. Mater.* 11(4):311–15
142. Marbella LE, Zekoll S, Kasemchainan J, Emge SP, Bruce PG, Grey CP. 2019.  $^7\text{Li}$  NMR chemical shift imaging to detect microstructural growth of lithium in all-solid-state batteries. *Chem. Mater.* 31(8):2762–69
143. Poggio M, Herzog BE. 2018. Force-detected nuclear magnetic resonance. In *Micro and Nano Scale NMR: Technologies and Systems*, ed. J Anders, JG Korvink, pp. 381–420. Weinheim, Ger.: Wiley-VCH Verlag
144. Nichol JM, Naibert TR, Hemesath ER, Lauhon LJ, Budakian R. 2013. Nanoscale Fourier-transform magnetic resonance imaging. *Phys. Rev. X* 3(3):031016. Erratum. 2013. *Phys. Rev. X* 3(4):049901
145. Dalladay-Simpson P, Howie RT, Gregoryanz E. 2016. Evidence for a new phase of dense hydrogen above 325 gigapascals. *Nature* 529(7584):63–67
146. Harris KDM. 2016. New in situ solid-state NMR strategies for exploring materials formation and adsorption processes: prospects in heterogeneous catalysis. *Appl. Petrochem. Res.* 6(3):295–306
147. Hughes CE, Williams PA, Harris KDM. 2014. “CLASSIC NMR”: an in-situ NMR strategy for mapping the time-evolution of crystallization processes by combined liquid-state and solid-state measurements. *Angew. Chem. Int. Ed.* 126(34):9085–89
148. Hughes CE, Walkley B, Gardner LJ, Walling SA, Bernal SA, et al. 2019. Exploiting in-situ solid-state NMR spectroscopy to probe the early stages of hydration of calcium aluminate cement. *Solid State Nucl. Magn. Reson.* 99:1–6
149. Walter ED, Qi L, Chamas A, Mehta HS, Sears JA, et al. 2018. *Operando* MAS NMR reaction studies at high temperatures and pressures. *J. Phys. Chem. C* 122(15):8209–15
150. Chamas A, Qi L, Mehta HS, Sears JA, Scott SL, et al. 2019. High temperature/pressure MAS-NMR for the study of dynamic processes in mixed phase systems. *Magn. Reson. Imaging* 56:37–44
151. Meier T. 2018. At its extremes: NMR at giga-Pascal pressures. *Annu. Rep. NMR Spectrosc.* 93:1–74
152. Huang Q, Tran KN, Rodgers JM, Bartlett DH, Hemley RJ, Ichiye T. 2016. A molecular perspective on the limits of life: enzymes under pressure. *Condens. Matter Phys.* 19(2):22801
153. Meier T, Wang N, Mager D, Korvink JG, Petitgirard S, Dubrovinsky L. 2017. Magnetic flux tailoring through Lenz lenses for ultrasmall samples: a new pathway to high-pressure nuclear magnetic resonance. *Sci. Adv.* 3(12):eaao5242
154. Meier T, Khandarkhaeva S, Petitgirard S, Körber T, Lauerer A, et al. 2018. NMR at pressures up to 90 GPa. *J. Magn. Reson.* 292:44–47

155. Edwards T, Endo T, Walton JH, Sen S. 2014. Observation of the transition state for pressure-induced  $\text{BO}_3 \rightarrow \text{BO}_4$  conversion in glass. *Science* 345(6200):1027–29
156. Gaudio SJ, Edwards TG, Sen S. 2015. An in situ high-pressure NMR study of sodium coordination environment compressibility in albite glass. *Am. Mineral.* 100(1):326–29
157. Sorte EG, Banek NA, Wagner MJ, Alam TM, Tong YJ. 2018. In situ stripline electrochemical NMR for batteries. *ChemElectroChem* 5(17):2336–40
158. Pecher O, Bayley PM, Liu H, Liu Z, Trease NM, Grey CP. 2016. Automatic tuning matching cyclers (ATMC) in situ NMR spectroscopy as a novel approach for real-time investigations of Li- and Na-ion batteries. *J. Magn. Reson.* 265:200–9
159. Pecher O, Halat DM, Lee J, Liu Z, Griffith KJ, et al. 2017. Enhanced efficiency of solid-state NMR investigations of energy materials using an external automatic tuning/matching (eATM) robot. *J. Magn. Reson.* 275:127–36
160. Koczor B, Sedyó I, Rohonczy J. 2015. An alternative solution for computer controlled tuning and matching of existing NMR probes. *J. Magn. Reson.* 259:179–85
161. Deleted in proof
162. Kobayashi T, Pruski M. 2019. Spatial distribution of silica-bound catalytic organic functional groups can now be revealed by conventional and DNP-enhanced solid-state NMR methods. *ACS Catal.* 9:7238–49
163. Griffith KJ, Wiaderek KM, Cibin G, Marbella LE, Grey CP. 2018. Niobium tungsten oxides for high-rate lithium-ion energy storage. *Nature* 559(7715):556–63
164. Deleted in proof
165. Ilott AJ, Mohammadi M, Schauerman CM, Ganter MJ, Jerschow A. 2018. Rechargeable lithium-ion cell state of charge and defect detection by in-situ inside-out magnetic resonance imaging. *Nat. Commun.* 9(1):1776

# Contents

## Data-Driven Discovery of Materials

- Evolving the Materials Genome: How Machine Learning Is Fueling  
the Next Generation of Materials Discovery  
*Changwon Suh, Clyde Fare, James A. Warren, and Edward O. Pyzer-Knapp* ..... 1
- Machine Learning for Structural Materials  
*Taylor D. Sparks, Steven K. Kauwe, Marcus E. Parry, Aria Mansouri Tehrani,  
and Jakob Brgoch* ..... 27
- Machine Learning in Materials Discovery: Confirmed Predictions  
and Their Underlying Approaches  
*James E. Saal, Anton O. Oliynyk, and Bryce Meredig* ..... 49
- Opportunities and Challenges for Machine Learning in Materials  
Science  
*Dane Morgan and Ryan Jacobs* ..... 71

## Quantum Materials and Devices

- Microwave Microscopy and Its Applications  
*Zhaodong Chu, Lu Zheng, and Keji Lai* ..... 105
- Angle-Resolved Photoemission Spectroscopy Study of Topological  
Quantum Materials  
*Chaofan Zhang, Yiwei Li, Ding Pei, Zhongkai Liu, and Yulin Chen* ..... 131
- Epitaxial Growth of Two-Dimensional Layered Transition Metal  
Dichalcogenides  
*Tanushree H. Choudbury, Xiaotian Zhang, Zakaria Y. Al Balushi,  
Mikhail Chubarov, and Joan M. Redwing* ..... 155

## Current Interest

- Morphology-Related Functionality in Nanoarchitected GaN  
*Abhijit Chatterjee, Shashidhara Acharya, and S.M. Shivaprasad* ..... 179
- Multiscale Patterning from Competing Interactions and Length Scales  
*A.R. Bishop* ..... 207

Spontaneous Ordering of Oxide-Oxide Epitaxial Vertically Aligned Nanocomposite Thin Films <i>Xing Sun, Judith L. MacManus-Driscoll, and Haiyan Wang</i> .....	229
Antisymmetry: Fundamentals and Applications <i>Hari Padmanabhan, Jason M. Munro, Ismaila Dabo, and Venkatraman Gopalan</i> ....	255
Energy Conversion by Phase Transformation in the Small-Temperature-Difference Regime <i>Ashley N. Bucsek, William Nunn, Bharat Jalan, and Richard D. James</i> .....	283
Hybrid Thermoelectrics <i>Jia Liang, Shujia Yin, and Chunlei Wan</i> .....	319
Noble Metal Nanomaterials with Nontraditional Crystal Structures <i>Chaitali Sow, Suchithra P, Gangaiab Mettela, and Giridhar U. Kulkarni</i> .....	345
Muon Spectroscopy for Investigating Diffusion in Energy Storage Materials <i>Innes McClelland, Beth Johnston, Peter J. Baker, Marco Amores, Edmund J. Cussen, and Serena A. Corr</i> .....	371
High-Energy X-Ray Diffraction Microscopy in Materials Science <i>Joel V. Bernier, Robert M. Suter, Anthony D. Rollett, and Jonathan D. Almer</i> .....	395
Frontiers in the Simulation of Dislocations <i>Nicolas Bertin, Ryan B. Sills, and Wei Cai</i> .....	437
Grain Boundary Complexion Transitions <i>Patrick R. Cantwell, Timofey Frolov, Timothy J. Rupert, Amanda R. Krause, Christopher J. Marvel, Gregory S. Rohrer, Jeffrey M. Rickman, and Martin P. Harmer</i> .....	465
Recent Advances in Solid-State Nuclear Magnetic Resonance Techniques for Materials Research <i>Po-Hsiu Chien, Kent J. Griffith, Haoyu Liu, Zhehong Gan, and Yan-Yan Hu</i> .....	493
Self-Assembly of Block Copolymers with Tailored Functionality: From the Perspective of Intermolecular Interactions <i>Rui-Yang Wang and Moon Jeong Park</i> .....	521
Thermoelectric Properties of Semiconducting Polymers <i>Kelly A. Peterson, Elayne M. Thomas, and Michael L. Chabinyc</i> .....	551
<b>Indexes</b>	
Cumulative Index of Contributing Authors, Volumes 46–50 .....	575

## Errata

An online log of corrections to *Annual Review of Materials Research* articles may be found at <http://www.annualreviews.org/errata/matsci>